Politecnico di Torino
Dipartimento di Elettronica e Telecomunicazione - DET

Master's degree in Nanotechnologies for the ICTs

Development of highly sensitive piezoresistive sensor exploiting PDMS-infiltrated 3D graphene sponge

Author:
Rossella Galli

Relators:
Prof. Marco Sangermano
Dr. Andrea Lamberti
Dr. Vittorio Morandi
Dott.ssa Fabiola Liscio

December, 2019

Contents

1. Introduction

Recent years have shown a significant progress in the development of stretchable electrodes which remain the key building block in flexible and stretchable electronic devices. One of the basic requests for these devices is the preservation of basic of their essential function under different mechanical deformations. Stretchable electrodes based on organic materials are highly flexible, stretchable, lightweight and inexpensive. For this reasons, they have attracted great attention in particular for use in soft electrodes [1].
The objective of this thesis is to illustrate the results of the fabrication and electrical characterization of highly sensitive PDMS infiltrated 3D graphene sponge realized in collaboration between the Politecnico di Torino and the CNR of Bologna as materials for high sensitive piezoresistive sensors. Indeed, piezoresistive sensors are based on the change in electrical resistivity of a material when it is deformed. Many materials show piezoresistivity, but only those with a high sensitivity are suitable to be used as sensors [2].

This study deals with the possible sensing applications of three-dimensional foam-like graphene structures. Starting from a commercial Ni porous structure, the deposition of graphene is performed by Chemical Vapour Deposition (CVD). Then, in order to guarantee mechanical support for the successive steps, Poly-Methyl MethAcrylate (PMMA) is infiltrated and, successively, the Ni is etched. In this way, a hollow free-standing graphene foam with pores filled with PMMA is formed. Subsequently, by infiltrating a polymer into the hollow graphene structure, it is possible to obtain a three-dimensional (3D) graphene foam (GF)/polydimethylsiloxane (PDMS) composite. At the end of the process, PMMA is removed in an acetone solution.
During the years, it has been observed that PDMS and epoxy resins are the major candidates to reinforce the graphene foam filler. The good electrical and mechanical proprieties derived from the GF/PDMS composities combined with the structure of GFs leads to a great potential for the use as flexible and stretchable conductors in a wearable communication devices. In fact, it can bend, stretch and twist without breaking the structure.

The possible advantages of 3D graphene foam are: low mass density, large surface area, high electrical conductivity due to the fact that GFs are constitute by continuous graphene layers that allow fast charge transport. More in details, the electrical conductivity of GF/PDMS is increased of 6 orders of magnitude with respect to the value derived from graphene-based composites and also is higher than those obtained from the carbon nanotubes (CNT). For what concerns the mechanical properties, the ultimate strenght of this structure is increased by a factor 1.3 compared with the pure PDMS [3]. The main problems encountered in GF/PDMS are: the weak interfacial interaction between graphene and polymer matrix, the non-uniform distribution of graphene sheets within the polymer and finally low quality and/or high inter-sheet junction contact resistance.[4]
The unique network structure, high specific surface area and outstanding electrical and mechanical properties of GF foam permit different applications, such as high-performance electrically conductive polymer composites or electrode materials for supercapacitors.

This fabrication technique guarantees many degrees of freedoms: for example, by tuning the porosity of the Ni scaffold, the network and pore structures of GFs can be easily tailored. Moreover, by performing the CVD processes, it is possible to obtain different thicknesses changing the deposition time and the precursor concentration. Indeed, a higher methane (CH_4) concentration leads to an increase in the number of graphene layers and this results in a difference in the specific surface area, density and electrical conductivity of GFs.

As mentioned before, the excellent properties of graphene have made it an excellent candidate for the next generation of flexible electronics applications. However, the graphene-based technology has specific challenges to overcome, namely, first, the difficulty of dispersing the graphene into the polymer matrix, and, secondly, the possible severe deterioration of the graphene structure under mechanical deformation. The first challenge is related to the high graphene aspect-ratio and to the surface interaction between graphene layers and the polymer matrix, that can cause the detachment of the graphene layers from the matrix. Indeed, polymers reinforced with graphene present various discontinuity zones that influence their overall behavior. From the atomic point of view, the carbon atoms within the graphene planes are hold together by aromatic bonds which are responsible for the chemical stability and inertness of graphene. On the other side, graphene interacts with the polymers through the weak intermolecular forces and the result is the low interfacial bond strength between graphene layers and the polymer matrix. The combination of the covalent bond of the polymer and the weak intermolecular forces among graphene layers give low surface energy between the two components [5], and this leads to inhomogeneities in the structure of the composites. Within this framework, PDMS has attracted great attention in the last years, thanks to an excellent surface chemistry with graphene, that allows to reduce the impact of the limitations discussed above, and, therefore, more reproducible and stable composites. For what concerns the second challenge, generally speaking, the mechanical deformation must be typically limited, in order to keep the electrical response reproducible and reversible. Indeed, for very large deformations, it has been observed that the conductivity gradually decreases, due to the progressive cracking of the graphene conductive network. A polymer substrates may help to overcome this limitation as it allows to improve the deformation distribution and gives to the structure an high degree of recoverable deformability [2]. For the reasons highlighted above, a PDMS scaffold seems to be the best candidate to try to overcome also this limitation.

Thesis content

This section is useful to provide to the reader a general overlook on how the thesis is structured in order to fully understand the work and show its significance in above highlighted field. After the Introduction, in Chapter 1, the properties of the employed materials are described in details, defining their role in the presented study. In Chapter 2 the characterization and materials production methods are reported and explained. The fabrication process of the foams is then illustrated in Chapter 3, followed by the discussion of the results coming from the characterization of each fabrication step. In Chapter 4 the electrical measurements performed were discussed by focusing on different aspects such as the response of the material when it is subjected to a compressive stress, bending and the change in temperature. Conclusions section is then is dedicated to a brief recap of the overall work, to the achievements of the present work, followed by ideas and thoughts for possible studies and future research activities.

2. Materials

In this chapter, it is reported the materials explotation in order to realize the highly sensitive piezoresistive sensor based on PDMS infiltrated 3D graphene foam. Firstly, the main characteristic of the Nickel scaffold is analyzed. Then the properties and structure of graphene are taken into consideration, and finally, the two polymers employed are discussed.

2.1 Nickel Foam

Foam materials are produced in a wide range of polymers, metals, and composites having either solid or tubular ligaments. The metals foams include aluminium, nickel, copper, silver, zinc, leads, and stainless steel. A particular characteristic of metal foams is that they maintain some physical properties of their base material.
A metal foam is a structure made of a solid metal that contains a large volume fraction of gas-filled pores. In particular, pores can be sealed in closed-cell foam or can form an interconnected network and called an open-cell foam. Open-pore metals foam are constituted by a metallic network of single struts which provide the stochastically distribution of cells and gas can pass the material. In the close-pore metal foams, the metallic portion separate a single fluid-filled cells.
Porous metals, due to their structure, are lightweight materials with good specific strength, stiffness and processability that make them an excellent candidate for engineering purposes. In this way it is possible to find many application in different fields such as aerospace, electronics and communications, electrochemistry, and bioengineering since porous materials possess both functional and structural characteristic. As a consequence, the possible applications related to its properties are mechanical dumping, vibrational control, acoustic absorption, energy and thermal management, and biocompatible inserts.
Compared to dense solid metals, porous one possess additional properties like low density, large specific surface area, and reasonable energy absorption. Typically, the value of the percentage of void in a metal foam is 75-95% [6]. Thanks to the large specific surface area, metal foams are useful to fabricate electrodes, catalysis, capacitors, and heat exchangers [7].
A metal foam is characterized structurally by the following parameters:

- the material from which it is constituted;
- relative density: ratio of density ρ and density of solid material of the cell wall ρ_s;
- cell size, cell shape and anisotropy;
- cell topology (open or closed cells) [8].

High and uniform macropores structure is the characteristic of Nickel foams; in this way, they possess a sizeable supporting area. The Nickel foam scaffold is a 3D porous structure with hollow branches and circular pores. Nickel foam possesses many features typically of metal foams, such as exceptional

uniformity, ultra-light material, high porosity, intrinsic strength, corrosion resistance, and good electrical and thermal conductivity. In table 2.1 the main properties of Ni-foam are reported :

PROPERTIES	**SYMBOL**	**UNIT**	**VALUE**
Density	ρ	Mg/cm^3	0.26 - 0.37
Relative density	ρ_s	-	0.03 - 0.04
Structure	-	-	Open cell
Melting point	T_m	K	1700 - 1720
Specific heat	c_p	J/Kg K	450 - 460
Thermal cond.	λ	W/m K	0.2 – 0.3
Young's modulus	E	GPa	0.4 - 1.0
Poisson's ratio	ν	-	0.31 - 0.34
Resistivity	R	10^{-8} ohm m	300 – 500

Table 2.1: Properties of Ni-foam

2.2 Graphene

In nature, carbon is present in many allotropes forms, as diamond, graphite, fullerene and nanotubes. Starting from the first type, diamond possesses a tetrahedral structure in which each single carbon atom is hybridized sp^3 and is linked to the other four nearest neighbours. A diamond cubic structure is formed by two interpenetrating face-centred cubic lattices in which one is displaced by one-quarter of the diagonal along with a cubic cell. This particular rigid structure give rise to many important properties such as high hardness, high thermal conductivity, low thermal expansion coefficient and high resistance to any chemical agent (including strong acids and bases) at room temperature.
The second allotrope form is graphite, in which the structure is composed by a multilayer parallel sheet where the carbon atoms are hybridized sp^2, and form a 2D honeycomb-like lattice. The typical characteristic is that among one plane and another there is Van der Waals force, and in this way, each layer can easily slide. Due to this fact, graphite is an anisotropic material: it is conductive along the direction of the plane, but it is an insulator in the perpendicular one.
In 2004 two researchers of the University of Manchester, Geim and Novoselev, isolate the superficial monolayer sheet of graphite, called graphene. In particular, thanks to its peculiar properties such as structural, electrical, thermal, optical and mechanics, this material became the focus of research during the following years. An example of possible applications regards energy (electrodes of energy storage device), sensors (chemical and biological sensors), fillers in conductive polymeric composites but also electromagnetic and optoelectronics implementation. Graphene is just the first one of a new class of materials that are only one atom thick. These so-called two-dimensional (2D) materials extend in only two dimensions: length and width; the third one, height, is considered to be zero [9].
Graphene can be considered as the primary building block for various other carbon allotropes forms, in fact, it can be wrapped up into fullerene (0D), rolled up into carbon nanotube (1D) and stacked up into many layers graphite (3D), as mentioned before (figure 2.1). Moreover, the fullerene structure is close and hollow, typically like a sphere, or a ellipsoid, or even a tube and/or a nanotube [10].
Graphene can be synthesized through different methods: mechanical exfoliation, chemical synthesis, epitaxial growth on Silicon Carbide and chemical vapour deposition. The latter is the most used techniques to obtain high-quality graphene on a large scale.

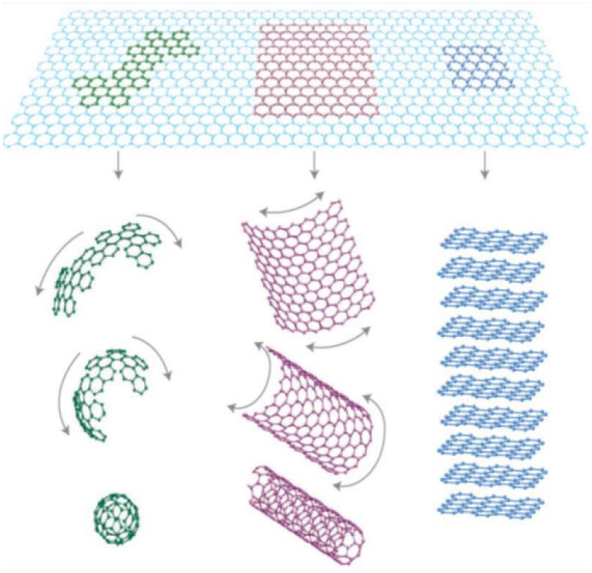

Figure 2.1: Graphene is a 2D building materials of all other dimensionalities. It possible to be cut and folded into a spherical shape to make fullrene (0D), rolled up into carbon nanotubes (1D), or stacked on top of each other to transform into graphite (3D) [11].

2.2.1 Properties and applications

The main properties of graphene are [12]:

- **Atomic thickness**: the distance between on monolayer and another is about 0.335 nm;
- **Surface area**: high theoretical specific surface area-to-volume ratio equal to 2630 m^2g^{-1} without affecting significant the mechanical properties;
- **Electron mobility**: high intrinsic charge mobility equal to 200000 $cm^2V^{-1}s^{-1}$, at high room temperature electron mobility due to the planar π-bonding, allow to excellent electrical conductivity (greater than silver);
- **Electrical resistivity**: 1 x 10^8 Ω m ($\sim$ 35 % less than Cu);
- **Strenght**: the defect-free monolayer graphene posses an exceptional mechanical properties with a breaking strength of $\sim$ 40 N/m, intrinsic strenght of 130 GPa
- **Stiffness**: high Young's modulus: 1 TPa;
- **Thermal conductivity** of a suspended graphene sheet at room temperature in the range 4.84 x 10^3-5.3 x 10^3 $Wm^{-1}K^{-1}$;
- **Transparency**: graphene absorbs 2.3 $\pm$ 0.1% of light independent on the wavelength and it posses an high transmittance of 97.7%;
- **Impermeability**: even the smallest atom as Helium cannot pass through a sheet of graphene;
- **Chemistry**: graphene sheet can be funzionalized with other elements to achieve heterogeneous chemical and electronic structures.

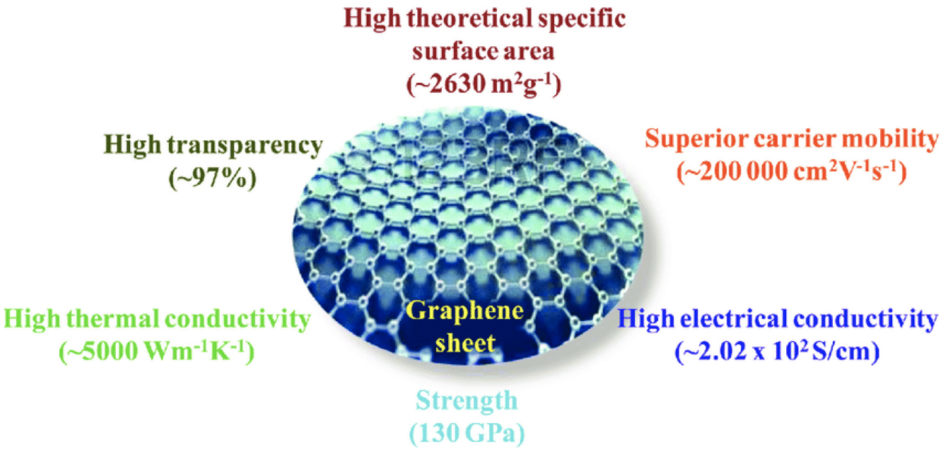

Figure 2.2: Properties of graphene sheet
[12]

Graphene's unique combination of excellent properties offers a material platform for the development of next-generation technologies in different areas (figure 2.3). In **electronics applications**, thanks to the arrangement of the carbon atoms, the electron can easily travel at high velocity without scattering. In this way, they do not lose energy, and so the conduction is high. Thanks to this it is possible to fabricate high frequency electronics and high-performance transistors, and, thanks to the combination of the above highlighted properties, stretchable and foldable devices and low-cost printable electronics

are produced.
Another important field in which this material can be exploited is for **energy harvesting and storage**. In particular in four areas: solar cells, supercapacitors, graphene batteries and catalysis for fuel cells.
The mechanical properties are suitable as a reinforcing agent in **composites and coatings**. Graphene with its low mass and low loading requirement is a good candidate for superhydrophobic coatings, corrosion protection, transparent conductive coatings for photonic devices and lightweight composites for body structure.
The impermeability of this material leads to the electrical control of water flow through graphene **membranes**, gas barrier in food packaging and water purification and desalination. In particular, a single layer of atoms can act as a barrier when dealing with liquid and gases. Therefore graphene can selectively allow the transport of gas and water molecules.
Graphene is also paving the way for novel **biomedical technologies** due to its high surface area. In particular, for bioelectronics, targeting and neutralizing cancer stem cells but also for luminescent graphene tags for bioimaging.
In conclusion, because every carbon atom is exposed to its environment, it is an ideal material for biological gas and chemical **sensors**.

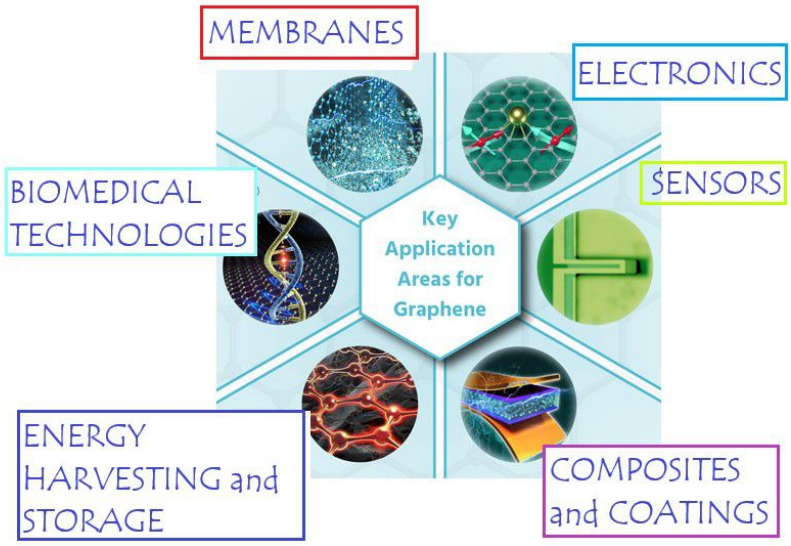

Figure 2.3: Different areas of graphene

2.2.2 Crystal structure

The crystal structure of graphene is constituted by a carbon atoms arranged in an hexagonal lattice in a plane, indeed they forming the so called honeycomb lattice.

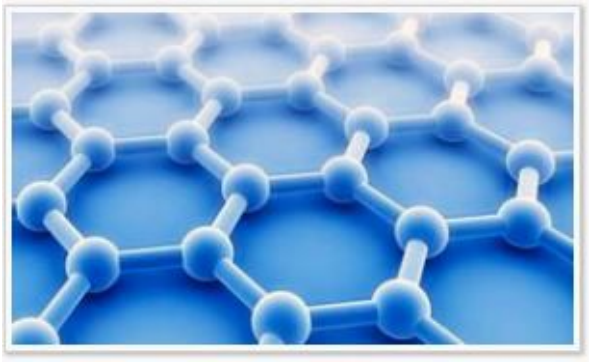

Figure 2.4: Honeycomb structure of graphene

The electron configuration of the carbon in its ground state is $1s^2\ 2s^2\ 2p^6$. From the electronic configuration it is possible to notice that the ground state carbon doesn't have enough unpaired electrons to bond with other three carbon atoms and in this way to form graphene. The carbon atom has to excite one of the electrons in the $2s^2$ pair into one of the empty $2p$ orbitals. Now, the electronic configuration becomes: $1s^2\ 2s^1\ 2p^3$ and the carbon atom is said to be in an excited state (figure 2.5). In particular, the $2s^1$ electron and two of $2p^3$ electrons are hybridized into sp^2 orbitals identified as 2s, $2p_x$ and $2p_y$.

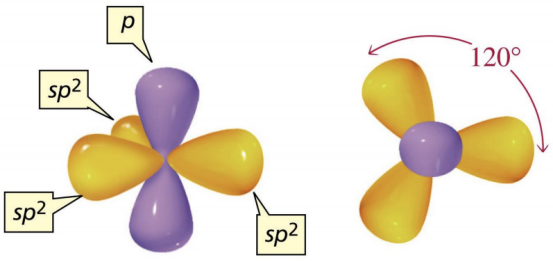

Figure 2.5: sp^2 hybridization [13]

The sp^2 hybridization between one s orbital, and two p orbitals lead to a triagonal planar structure with a formation of a covalent σ bond (the three sp^2) between carbon atoms that are separated each other 1.42 Å (lattice constant). Moreover, the σ band is responsible for the robustness of the lattice structure. The remaining $2p$ orbital, which is perpendicular to the planar structure, can form a covalent bond with neighbouring carbon atoms, leading to the formation of a π band. Moreover, the π-bonds are hybridized together to form the π-band and the π^*-bands that contribute to a delocalized network of electrons, since each p orbital has one extra electron [13].

The unit cell of graphene is formed by two carbon atoms, while the graphene lattice is constituting of two sublattices which represent the triangular Bravais lattice. A graphene sheet forms a two-dimensional hexagonal crystal lattice with a primitive cell that contains two atoms. Lastly, the lattice structure has a basis of two atoms per unit cell (A and B), (figure 2.6).

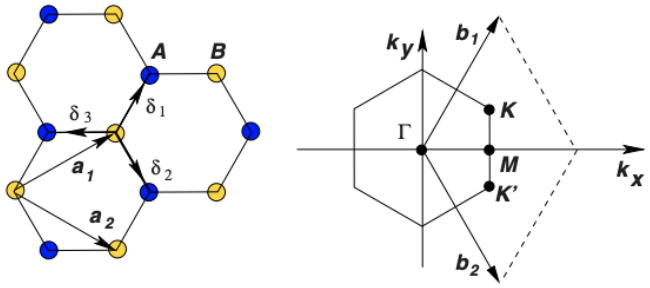

Figure 2.6: Graphene hexagonal crystal lattice and First Brillouin zone of graphene strucure

To construct the reciprocal lattice, firstly the primitive cell has to be determined and then by translational symmetry, the whole lattice of graphene is recovered. The basis vectors of the triangular Bravais lattice are (a is the lattice unit cell):

$$a_1 = \frac{a}{2}(3, \sqrt{3}) \tag{2.1}$$

$$a_2 = \frac{a}{2}(3, -\sqrt{3}) \tag{2.2}$$

The reciprocal lattice vector are represented as:

$$b_1 = \frac{2\pi}{3a}(1, \sqrt{3}) \tag{2.3}$$

$$b_2 = \frac{2\pi}{3a}(1, -\sqrt{3}) \tag{2.4}$$

The nearest-neighbor vector are:

$$\delta_1 = \frac{a}{2}(1, \sqrt{3}) \tag{2.5}$$

$$\delta_2 = \frac{a}{2}(1, -\sqrt{3}) \tag{2.6}$$

$$\delta_3 = -a(1, 0) \tag{2.7}$$

The positions in the momentum space of the Dirac points are given by:

$$K = (\frac{2\pi}{3a}, \frac{2\pi}{3\sqrt{3}a}) \tag{2.8}$$

$$K' = (\frac{2\pi}{3a}, -\frac{2\pi}{3\sqrt{3}a}) \tag{2.9}$$

2.2.3 Band structure

In order to study the electronic band structure of graphene, the Hamiltonian has to be determined. As mentioned before, all σ-orbits of carbon atoms are responsible for strong bonds in the graphene plane. Moreover, the conductive properties of the sheet are related to the π-orbitals that are perpendicular to the plane. The electronic band structure of graphene can be described by using the **tight-binding model**. When the distance that separates the neighbour atoms is bigger than the Bohr's radius, this approximation is valid. Considering only nearest-neighbour hopping the tight-binding Hamiltonian for graphene is:

$$\widehat{H} = -t \sum_{<ij>} (\widehat{a}_i^\dagger \widehat{b}_j + \widehat{b}_j^\dagger \widehat{a}_i) \tag{2.10}$$

where the i, j indicates the sites in the sublattice A(B), then the fermionic operator $\widehat{a}_i^\dagger(\widehat{a}_i)$ creates (annihilates) an electron at the A site whose position is r_i, same for $\widehat{b}_j^\dagger(\widehat{b}_j)$. Moreover t is the nearest-neighbor hopping energy so it indicates the hopping between different sublattice and its value is approximately 2.8 eV.
It is possible to express the Hamiltonian as:

$$\widehat{H} = \sum_k \psi^\dagger h(k) \psi \tag{2.11}$$

where

$$\psi = \begin{pmatrix} \widehat{a}_k \\ \widehat{b}_k \end{pmatrix}, \qquad \psi = \begin{pmatrix} \widehat{a}_k^\dagger & \widehat{b}_k^\dagger \end{pmatrix} \tag{2.12}$$

and $h(k)$ is the matrix representation of the Hamiltonian equal to:

$$h(k) = -t \begin{pmatrix} 0 & \Delta_k \\ \Delta_k & 0 \end{pmatrix} \tag{2.13}$$

where

$$\Delta_k = \sum_\delta e^{ik\delta} \tag{2.14}$$

δ is the sum of the nearest-neighbor vectors δ_1,δ_2 and δ_3. By solving the eigenvalues problem is possible to find the eigenvalues solution of the matrix that are: $E_\pm = \pm t\sqrt{\Delta_k \Delta_k^*}$, where the minus sign applies to the valence π band that it is fully occupied (as mentioned before), while the plus sign is for the empty conduction π^* band (figure 2.7).
By computing the eigenvalues it is possible to obtain the energy dispersion relation:

$$E_\pm(k) = \pm t \sqrt{1 + 4cos\left(\frac{3}{2}K_x a\right) cos\left(\frac{\sqrt{3}}{2}K_y a\right) + 4cos^2\left(\frac{\sqrt{3}}{2}K_y a\right)} \tag{2.15}$$

or in short notation:

$$E_\pm(k) = \pm t\sqrt{3 + f(k)} \tag{2.16}$$

where:

$$f(k) = 2cos(\sqrt{3}k_y a) + 4cos\left(\frac{3}{2}k_x a\right) cos\left(\frac{\sqrt{3}}{2}k_y a\right) \tag{2.17}$$

In the figures 2.7 is reported the energy bands for graphene from nearest-neighbor interactions. The valence band and the conduction band forms a cone called Dirac cone at which they degenerate at the **Dirac points (K** and **K')** [14].

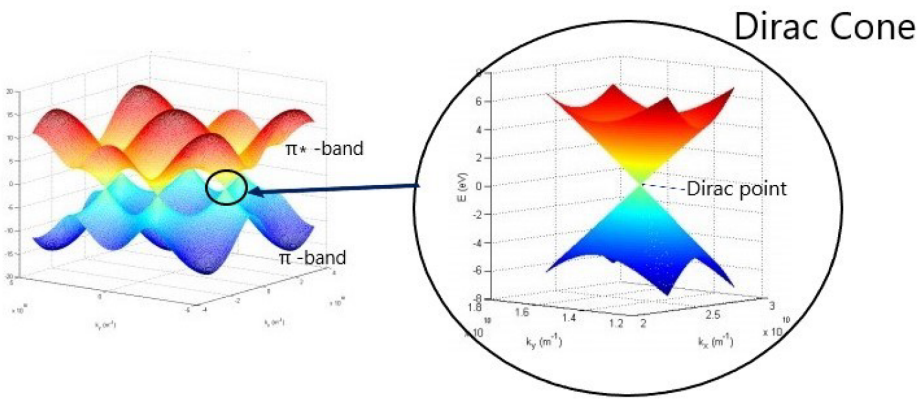

Figure 2.7: Band structure of graphene with details of conduction and valence band Dirac cone [15]. The Dirac points are the points in k-space for which $E_{\pm}(k) = 0$. [16]

Generally, the properties of the system are studied in the two Dirac points since the other vertex are equivalent to these sets (K and K'). Considering the behaviour of Δ_k at the Dirac point K and defining the relative momentum q as the difference between k and K it is possible to obtain:

$$\Delta_{k+q} = -ie^{-iK_x a \frac{3a}{2}(q_x + iq_y)} \tag{2.18}$$

in particular the phase of Δ_{k+q} carries no physical meaning and so can be neglected. As a consequence the Hamiltonian element is:

$$h(k) = v_F \begin{pmatrix} 0 & q_x + iq_y \\ q_x - iq_y & 0 \end{pmatrix} \tag{2.19}$$

where v_F is the characteristic velocity of the electron that in the case of graphene correspond to the Fermi velocity approximately equal to 1x10^6 m/s and it is given by:

$$v_F = \frac{3at}{2} \tag{2.20}$$

By expressing the Hamiltonian as a function of Pauli matrices is possible to obtain:

$$h(K + q) = v_F q\sigma \tag{2.21}$$

where $\sigma = (\sigma_x + \sigma_y)$ is the sum of the Pauli matrices.
Similarly for K', by defining the relative momentum $q = k - K'$ the Hamiltonian element can be written as:

$$h(K' + q) = v_F q\sigma \tag{2.22}$$

From the matrix form of Hamiltonian near the two Dirac points, it is possible to obtain the energy dispersion relation as:

$$E_{\pm}(q) = v_F |q| \tag{2.23}$$

In this way, it is demonstrated that the energy dispersion relation around the two Dirac points is linear and it corresponds to the dispersion relation of a relativistic Dirac fermion, as it is explained in the next section [15].

2.2.4 Electrical conductivity

In a semiconductor, the valence and conduction bands are separated by a narrow band gap that permits a significant number of electrons to overcome it by energy supplied. The main semiconductors have band edges that can be approximately by parabolic dispersion relation.
Consider graphene instead; as mentioned before, its structure is linked to its electrical properties. Moreover, the geometry and the electronic configuration of Carbon atom confer a peculiar electronic band structure with the results of exceptional mechanics and electrics properties.
The physics of graphene is determined by considering the energy spectrum at the so-called *point of neutral charge* that correspond to the six vertexes of the hexagon of FBZ (Dirac points). Here, as demonstrated above, the valence and conduction band touched themselves in single points, and as a consequence, the density of states at the Fermi level is zero (figure 2.8).

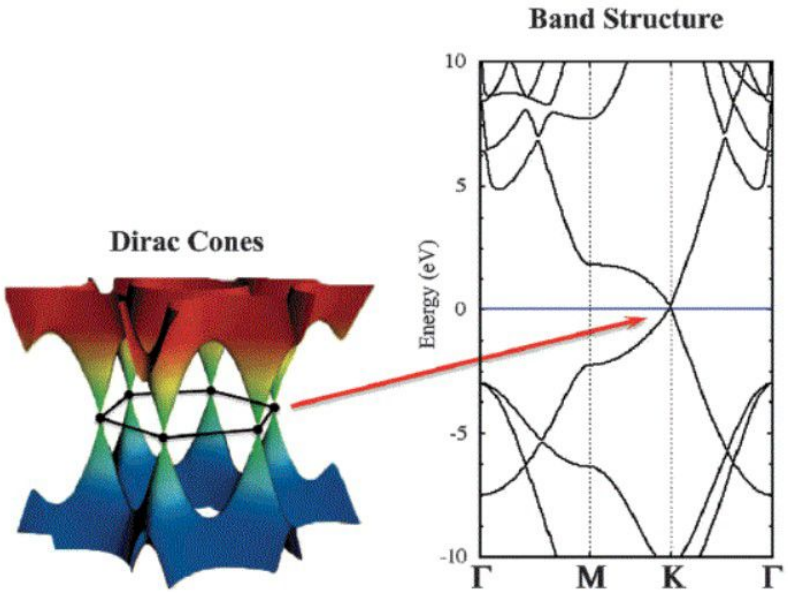

Figure 2.8: Graphene band structure (the blue line is the Fermi level) [17].

For a metal and a semiconductor, the electron kinetic energy in the effective mass approximation, is given by the equation:

$$E = \frac{p^2}{2m^*} \tag{2.24}$$

where p is the momentum, and m^* is the effective mass of the electron. This is in contrast with the energy dispersion relation found for graphene:

$$E = \left(\frac{h}{2\pi}\right) v_F k \tag{2.25}$$

where k is the particle momentum, h is the Plank constant, and v_F is the Fermi velocity.

Near the Dirac point, the bands assume a conic shape and the energy relation is linear, as mentioned before. Step away from these points the trend becomes not valid. Thus, an electron in graphene possesses an effective mass zero everywhere around the band edge except where the two bands are in touch, here it has an infinite effective mass.
The graphene's carriers at the Dirac points belong to a particular category of a relativistic quantum

particle: massless Dirac fermions. They are defined as **quasiparticles** described by a two-dimensional Dirac equation (cannot be described by the *Schrödinger equation*).
The conduction band of graphene is completely filled as in insulators, but at the Dirac point a single band is formed, and in this way, graphene behaves like a metal. So this material is defined as a **zero-gap semiconductor**.
It is experimental demonstrated that the conductivity of graphene tends to a minimum value even if the concentration of carriers tends to zero at the Dirac point [18]. This intrinsic characteristic belongs to Dirac fermions in 2D, it depends on the physics of the material and the relative quantum nature of the particle, but it is independent on the concentration of carriers, as they are electrons or holes.
Due to the conical shape of the bands, the carriers are massless and free to move without scattering with other atoms. In other words, electron-electron interactions are enhanced because of the absence of electronic screening and in this way, the conductivity rises.

2.3 Polymers

Polymers are covalently large molecules built starting from monomers, small structural units. The properties of a polymer are mainly dependent on the structure of individual polymer molecules, the shape and size and in particular, how they are arranged to form structure. Following how the chain it is composed they can be classified into: **homopolymer** (one species of monomer), **copolymer** (two monomer units), and finally, **terpolymer** (three different basic units).
There exist four main categories of copolymers (figure 2.9):

- Statistical copolymers: the distribution of the two monomers are random;
- Alternating copolymers: the monomers are placed in a regular way;
- Block copolymers: composed by a sequence or blocks;
- Graft copolymers: one is grafted on a blackbone and the other is part of branches.

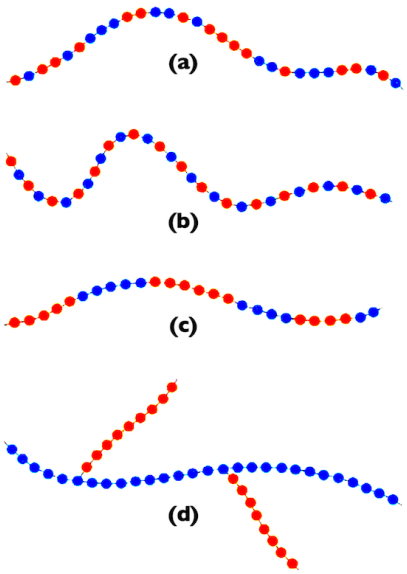

Figure 2.9: Different copolymers configurations: a) statistical b) alterating c) block d) graft [19]

Polymers can be formed by a chemical reaction in which a large numbers of monomers are joined sequentially to form a chain. Polymers are classified according to the reaction by which they are formed: addition and condensation. In the **addition polymerization**, all atoms of monomer became a part of the polymer, since there is no formation of reaction products. In this reaction an initiator is added in order to open the double bond between carbon atoms and in this way begins the linking process by adding more monomers to the chain. In the **condensation polymerization**, instead, some atoms of monomers are released into a small molecule.
In the reactions, monomers are linked together forming a covalent bond, also called *primary bond*. Between different chain, a weak *secondary bond* is formed such as van der Waals, hydrogen bonds or ionic bonds. During a polymerization reaction is not possible to assign an exact molecular weight to a polymer since random events determine the length of the chain. In particular, in a condensation reaction, the length is strongly dependent on the availability of the reactive group. While in the addition reaction, it depends on the lifetime of the chain carrier. For this reason, the product is a mixture of distribution of different length evaluated in a statistic way. In other words, in polymers,

the molar weight distribution is associated with a *molar weight distribution* instead of single molecular weight:

$$w_i = \frac{N_i M_i}{N_A} \tag{2.26}$$

where N_i is the number of molecules of species i of molecular weight M_i and N_A is the Avogadro's number (6,022 x 10^{23}). The higher is the molucular weight, the greater is its chain lenght.
It is also useful to describe the size of a polymer chain in terms of *degree of polymerization* (DP) defined as:

$$DP = \frac{molecular\ weight\ of\ polymer}{molecular\ weight\ of\ the\ repeating\ unit} \tag{2.27}$$

Moreover, higher is the DP; more significant will be the polymer's viscosity which can affect, for example, the overall cost processing. Besides, in a given polymers, the strength and viscosity increase with an increase of molecular weight: this is related from the fact that more extended is the polymer chain, more energy is required to overcome the strength of the secondary bond.
Polymers can also be classified into two different main classes (figure 2.10):

- **Thermoplastic**: are constituted by independent chains that are composed of atoms of carbon covalently bonded. From one chain to another, a weak secondary bond is present, and so they can be remelted and possess low melting points. **Thermoplastic elastomer** are class of copolymers that possess both thermoplastic and elastomeric properties. In this way, polymer hold viscoelasticity and weak intermolecular forces.
- **Thermosetting**: polymer in which is present a 3D lattice of covalent bonds. In particular, they are polymers that cross-link together during the curing process to form an irreversible chemical bond, so it remains in a permanent solid state once hardened. In this way, thermoset plastic products can withstand high temperature without losing austerity.

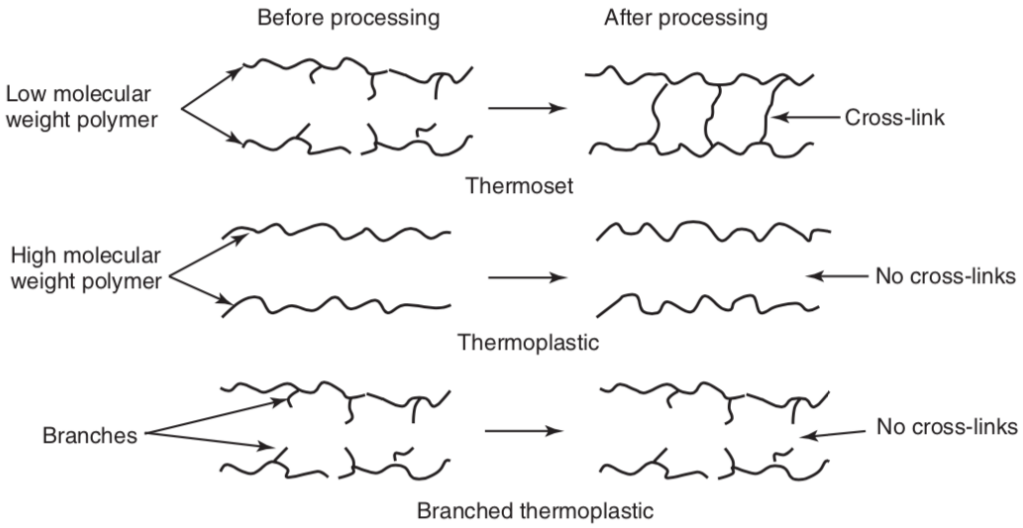

Figure 2.10: Classification between thermoset and thermoplastic strucures [19]

Two temperatures can be defined to characterize polymer properties. At low temperature, the polymers are rigid, hard and stable. Instead, when the temperature rises, polymer behave like a viscous liquid since it acquires enough thermal energy and so chains can easily slide over each other. The polymer can change from solid to liquid state in two ways, depending on the internal organization of the chains.

Different configurations are possible for polymers:

- **amorphous** (glass): the chain are arranged in a random way;
- **crystalline**: the chain are incorporated in an ordered 3D region;
- **semicrystalline**: a certain amount of amorphous region is present proportional of the crystalline part.

Moreover, it is possible to impart a different degree of crystallinity by controlling the rate of solidification during cooling, although polymer can never be 100% crystalline. Crystallinity influence mainly the physical and mechanical properties. When the degree of crystallinity increases, the polymer became harder, less ductile, less rubbery and as a consequence, it is more resistant to solvent and heat. *The melting temperature* T_m define the transformation from a solid to a viscous liquid upon heating. In amorphous and semicrystalline polymers, instead, *the glass transition temperature* T_g defines the transition between fragile and resistant to soft and flexible behaviour. In other words, it is a second-order transition and it represents the point at which essential properties change, such as specific volume, stiffness, refractive index, density, thermal conductivity and dielectric constant.

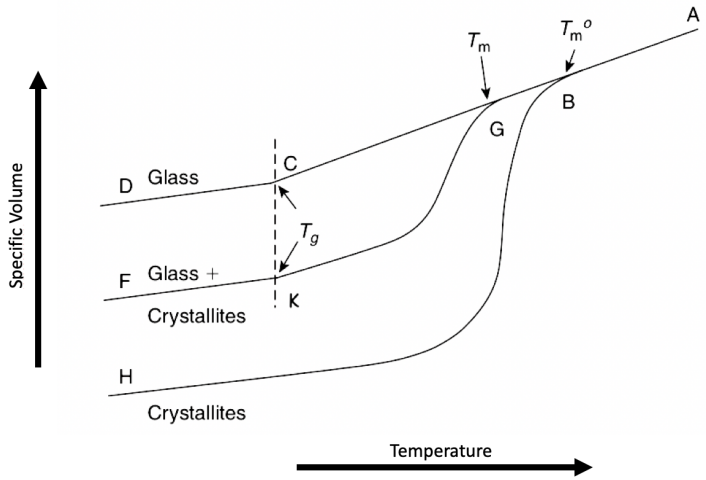

Figure 2.11: Change of a specific volume with temperature of different polymers [20]

Figure 2.11 reported different behaviour of polymers: amorphous polymer follows line ABCD. In C-D is glass, as the temperature increases the material change from rubbery to a viscous liquid state. The perfect crystalline polymer follows the curve HBA, and a semicrystalline polymer will run in FKGA curve. T_m^0 is the temperature at which the perfectly crystalline polymer melts and turn to a viscous state; it is lower than T_m [20].
An important equation to be introduced is the Flory-Fox equation that relates the average molecular mass of a polymer to its glass transition temperature:

$$T_g = T_{g,\infty} - \frac{K}{M_n} \tag{2.28}$$

where M_n is the molecular mass of polymer, and $T_{g,\infty}$ is the maximum value of T_g that can be reached at a theoretical molecular mass. K is an empirical parameter and it is related to the free volume present in the polymer sample. The free volume is an intrinsic proprierties of a polymer and is generated by the gaps left between entangled chains. Moreover, polymer with long channel (and so

high molecular mass) has less free volume with respect to the one with short chain. In the figure 2.12 is possible to notice the behaviour of T_g, in fact it increases with molecular mass and asymptotically approach to a maximum value.

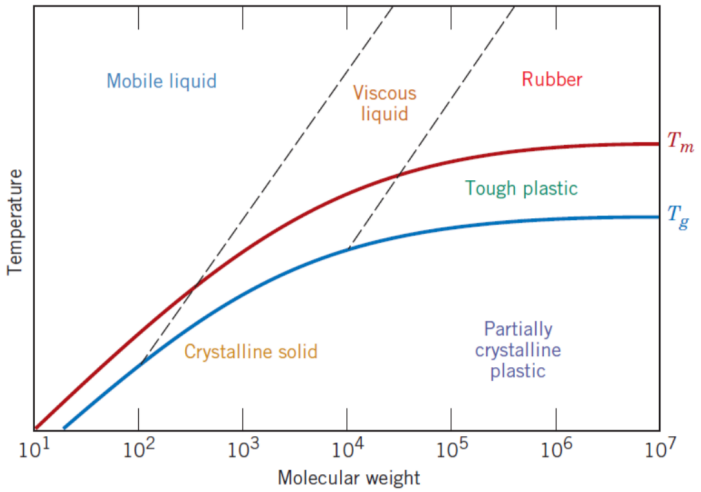

Figure 2.12: Effect of molecular weight on T_m and T_g [19]

Properties of polymers:

- low density;
- high plasticity;
- low melting temperature;
- flexible, deformable and low strength;
- soft and ductile;
- not stable at high temperature;
- optically translucent or transparent;
- good corrosion resistance.

Polymers present a band structure whose valance band is filled and separated from the empty conduction band by a large band gap (higher than 2 eV). When the temperature increases only few-electron may be excited and reach the conduction band. For this reason the quantity of free electrons in the structure is very low. This is the main reason why polymers possess a small value of electrical conductivity.

2.3.1 Poly-methyl methacrylate

Poly-methyl methacrylate (PMMA), also called acrylic, acrylic glass, or plexiglass (figure 2.13) is a transparent amorphous thermoplastic homopolymer. The presence of the methyl group CH_3 in the structure prevents it from packing closely in a crystalline arrangement, and from rotating freely around the C-C bonds [21]. Thermoplastic polymer materials are used in various applications due to their attractive properties like lightweight, cost, performance, and recyclability. The structure of thermoplastic is composed of weak secondary bonds between chains that permit to have a low effort flow on other chains of the same type. Moreover, a thermoplastic can be heated to its melting point, cooled and then reheated again without involving any degradation.

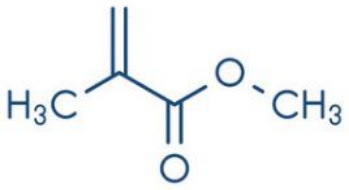

Figure 2.13: Structure of PMMA monomer [22]

The table report the main characteristics of PMMA:

PROPERTIES	
Formula	$C_5O_2H_8$
Density	1,17 $[g/cm^3]$
T_g	from 360 [K] to 430 [K]
T_m	-not applicable
T_c	-not applicable

PMMA possess the following properties [22]:

- lightweight;
- high resistance to sunshine exposure since it possess a small variation under UV-radiation;
- good thermal stability;
- high transparency and brilliance;
- mechanical properties, rigidity and dimensional stability and high impact strength;
- surface properties;
- hardness and high scratch resistance;

2.3.2 Poly-dimethylsiloxane

Poly-dimethylsiloxane (PDMS) (figure 2.14) is a non-entangled semi-crystalline silicon elastomer. It is polymeric organosilicon compound that belongs to a group of silicones with the chemical formula $CH_3[Si(CH_3)_2O]_nSi(CH_3)_3$ where n is the repeating monomer. PDMS possess weak intermolecular forces and high chain flexibility that lead to poor mechanical properties above the melting temperature. Moreover, after cross-linking process PDMS becomes a hydrophobic elastomer and can be molded to reproduce various structures down to nanoscale resolution.

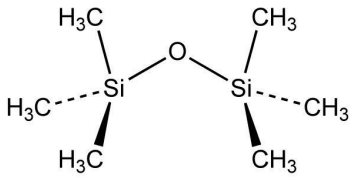

Figure 2.14: Chemical structure of PDMS [23]

The main characteristics of PDMS are reported in table below:

PROPERTIES	
Formula	$((CH_3)_2SiO)_n$
Density	0,970$[g/cm^3]$
T_g	150 [K]
T_m	236 [K]
T_c	173-183 [K]

PDMS possess the following characteristics:

- optically clear
- outstanding temperature and oxidative stability;
- excellent low temperature flexibility;
- low surface tension.

3. Analysis and Methods

3.1 Chemical Vapour Deposition

Chemical vapour deposition (CVD) [24] [25] [26] is a versatile process suitable for metal and non-metallic compounds such as carbon and silicon. The heterogeneous reaction is the base of this technique. It involves a change in state, in this case, from gaseous to solid form. The gaseous compound undergoes to a chemical reaction in order to deposit solid on the heated substrate. All CVD process need an energy supply source to break reactant gases into reactive species for deposition.
A generic process of CVD requires the deposition chamber to be performed in which a heated substrate is placed, and the gas molecules (precursor) are injected. The substrate also acts as a catalysis for the chemical reactions. The precursor molecules react with the substrate, and they deposit on it as a thin film. At the end of process, before cooled the sample the excess of the product ejected from the chamber.
CVD system is reported in figure 3.1, it is composed by:

- chemical source (gas);
- flow control to setting film parameters;
- reaction chamber with energy input;
- energy sources (heat, RF, optical).

Possible classifications of the CVD method are:

- Low pressure CVD (LPCVD): low pressure in the range of 5-250 Pa. The main advantages are excellent uniformity and purity; instead, it posses a low deposition rate.
- Atmospheric pressure CVD (APCVD): at ambient pressure and with very high deposition rates, and to small variations of temperature. Otherwise the possible drawbacks are poor uniformity and conformality, and finally, the purity is less than the one obtained from LPCVD.
- Plasma enhanced CVD (PECVD): in which the plasma is used as the energy supply. In the plasma, the species are electrically neutral, and they have incomplete bonding, and due to this fact, they are extremely reactive (radicals). The main advantages of this technique are the use of lower temperatures compared to LPCVD, good step coverage and density. On the contrary, the plasma can be extremely aggressive and can cause damages or chemical contaminants may occur.
- Metal-Organic CVD (MOCVD): used for II-VI and III-V group semiconductors and in particular for metallic oxides and metals.

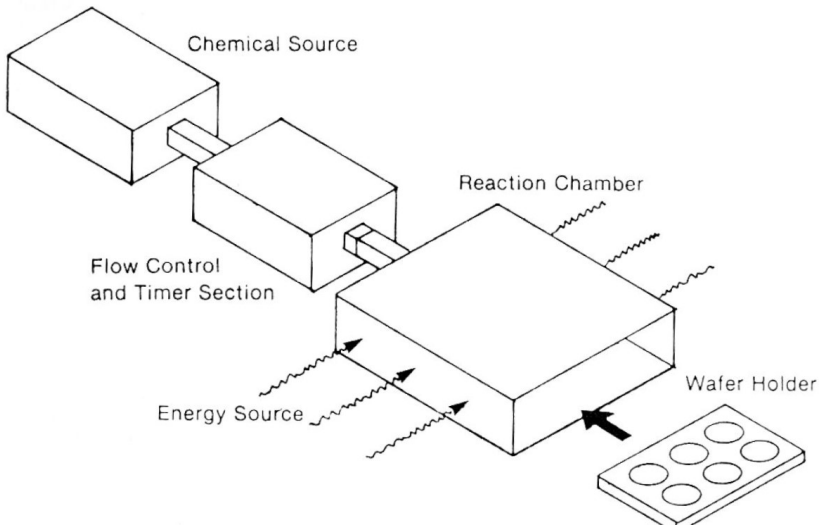

Figure 3.1: Basic CVD system

Moreover, two types of CVD system can be find depending if the substrate is heated:

- **Hot walls CVD**: in this type of CVD the all deposition chamber is heated and so also the substrate. Part of the reaction product can be deposited on the wall of chamber.
- **Cold walls CVD**: in this case only the substrate is heated and not the entire deposition chamber. In this sense, this is a more clean method in fact, the deposition products cannot reach the wall of the furnace chamber.

In a CVD reaction, two factors play an important role: thermodynamics and kinetics. The first is the driving force that governs the direction in which the reaction is going. Otherwise, the kinetics establish the transport process and the rate-control mechanism.
Additional important parameters are related to the chemistry of the reaction (the type of reaction, the correct choice of the precursor and reactant) and also the processing parameters like temperature and pressure.
In these techniques, four major steps are involved (figure 3.2):

- By forcing flow the reactant gases enter in the chamber and it diffuse to surface
- Chemical reaction takes place and as a consequence thin film is deposit on the surface
- After adsorption the reactive species can remain fixed at the surface site or it can migrate along the surface. This is temperature-dependent, and it affects the step coverage
- The products is desorbe and it diffuses from the surface

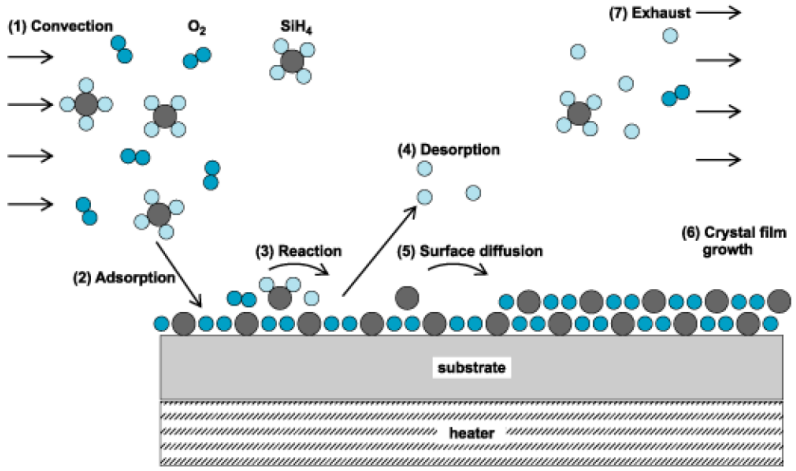

Figure 3.2: Reaction at the substrate surface

The reaction rate can limited any of this steps and it is defined in the equation 3.1 and it follow the Arrehnius law:

$$R = R_0 \exp\left(-\frac{E_a}{KT}\right) \tag{3.1}$$

Where R_0 is the reaction constant, E_a is the activation energy and KT is the thermal energy. The reaction flux is defined as in the equation 3.2:

$$j = \frac{DN_gR}{D + \delta R} \tag{3.2}$$

where D is the diffusion coefficient, N_g the concentration at the top of boundary layer and δ is the boundary layer thickness defined as the slow moving layer near the surface. Thus, the reaction rate became, equation 3.3:

$$r = \frac{j}{\gamma} = \frac{DN_gR}{\gamma(D + \delta R)} \tag{3.3}$$

where γ is the number of atoms per unit volume of reactant.
Moreover the surface reaction rate increases with increasing temperature and it saturates to a maximum, as it possible to notice from the graph below, equation 3.3:

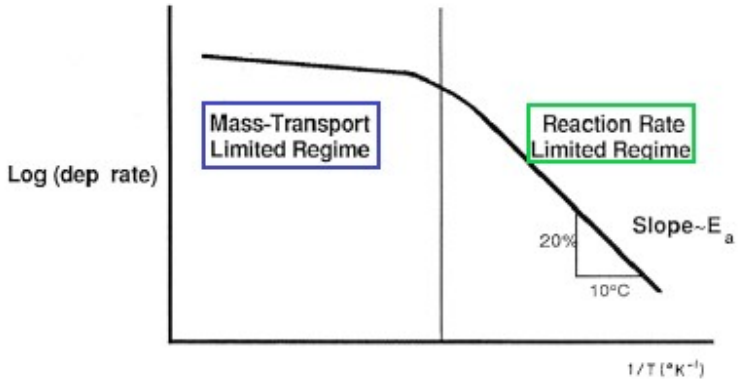

Figure 3.3: Temperature dependence of growth rate for CVD film. On the x-axis is reported the Temperature, otherwise on y-axis the deposition rate

At high temperatures, the mass transport is limited and the reaction rate is equal to, equation 3.4

$$r \approx \frac{DN_g}{\gamma\delta} \tag{3.4}$$

In this region, the surface reaction prevails over the diffusion, and thus, the diffusion of reactants limits the process. Due to this fact, there is a little change in a deposition with temperature.
For very low temperatures, instead the reaction rate is limited, and this means that in the formula prevails the diffusion rate over the surface reaction, equation 3.5:

$$r \approx \frac{N_g R}{\gamma} \tag{3.5}$$

In this part of the graph, the deposition rate changes rapidly with temperature: for example, at room temperature it changes 20% every 10 $°C$.

3.1.1 Graphene deposition

Graphene were synthesized by atmospheric pressure CVD, using the apparatus shown in figure 3.4. During this process, two different phases occur: precursor decomposition and graphitization.
The gas species are injected into the reactor, and they pass through the hot zone where the reaction of thermal decomposition (pyrolysis) of hydrocarbon happens:

$$\mathrm{CH_{4(g)}} \longrightarrow \mathrm{C_{(s)}} + 2\,\mathrm{H_{2(g)}}$$

Methane CH_4 decomposes into carbon radicals at the metal substrate surface, and then it forms a single-layer of graphene.

Figure 3.4: APCVD apparatus used for synthetize graphene

When the gas is injected into a chamber, a mass flow control measure the concentration, the composition and the flux of the precursor. The reactor is formed by a quartz tube of 5 cm diameter, and a section of 60 cm is cover by a series of a resistor in order to heat the chamber. A Venturi tube is used at the end of the process to remove the gas, by two different zones constitute it: one convergent and one is divergent, this latter is narrower with respect to the first side is the geometrical conformation allows the velocity to rise and consequently the pressure to be reduced.
During the deposition, the hydrogen H_2 is injected to acts as co-catalyzing to helps the bonding between carbon and substrate. However, the ration between CH_4 and H_2 has to be controlled, indeed, an excess of H_2 can decrease the velocity of the reaction, an excess of methane with respect to the hydrogen, can cause a reduction of the grown grain size.
In conclusion, the parameters that influences the quality of graphene are various: temperature, deposition time, concentration of the gas precursors, roughness and structure of the substrate. Figure 3.5, is a picture of several samples obtained after the graphene CVD using different deposition time and

precursors concentration. The different color is related with the different numbers of graphene layers grown on Ni surface.

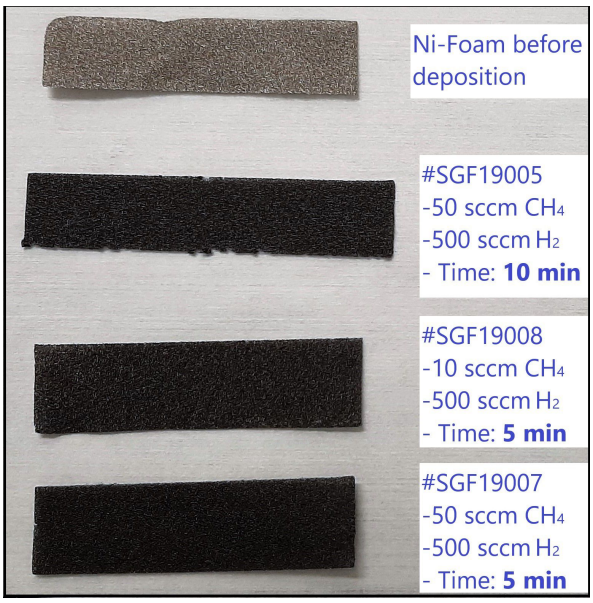

Figure 3.5: Picture shot on different samples obtained using the same Ni foam template but different CVD condition.

3.1.2 Deposition process

The graphene CVD process on Ni foam needs the following steps:

- **Intro**: the sample was inserted in the quartz tube at the external of the furnace.
- **Purge**: Nitrogen was injected to clean the chamber. In particular, in this process, was injected 100 sccm (Standard Cubic Centimeter per Minute) of gas. From now on inside the furnace, the pressure is equal to the one of the Venturi tube.
- H_2 **test**: H_2 was injected into the chamber to detect any gas leak by a gas sensor. In order to perform the test, the concentration of hydrogen was set to 200 sccm.
- **Sample insert**: the Nickel foam was inserted inside the chamber under H_2 flux of 50 sccm.
- **Thermal ramp**: the temperature was gradually increased until it reached $970°C$ inside the deposition chamber. This phase requires 1 hour.
- **Annealing**: during this step, the temperature was gradually increased and afterwards maintained up to 1000°C for 30 minutes.
- **Deposition**: the gas precursor (CH_4) and H_2 were injected in the chamber. The latter has a function to maintain the surface of Nickel free from oxide.
- **Rapid Extraction**: in this phase, carbon precipitated on the surface, and the graphene was formed.
- **Purge and Cool**: the sample was let inside the quartz tube in order to cool down. A constant flux of N was used to avoid the formation of amorphous carbon due to oxygen.

In the table 3.1 is reported the main step of the CVD process with the relative parameters of pressure, temperature, time and the flux of gases.

Step	**Pressure [Torr]**	**Temp. [°C]**	**time [min]**	CH_4 **[sccm]**	H_2 **[sccm]**	**N [sccm]**
1 - Intro	Amb	Amb	0	0	0	0
2 - Purge	Vent	Amb	10	0	0	1000
3 - H_2 test	Vent	Amb	10	0	200	0
4 - Sample ins.	Vent	Amb	1	0	50	0
5 - Th. ramp	Vent	↑ 1000	60	0	50	0
6 - Annealing	Vent	1000	30	0	50	0
7 - Deposition	Vent	1000	5	10	500	0
8 - Rapid Ext.	Vent	1000	1	10	500	0
9 - Purge & Cool	Vent	↓ *Cool*	120	0	0	150

Table 3.1: Graphene CVD recipes on Ni substrate

3.2 Scanning electron microscope and Energy-dispersive X-ray spectroscopy

Scanning electron microscope (SEM) (figure 3.6) is the most used type of electron microscope since it can provide, among others, information on size, shape, morphology, composition, crystallographic habit (under certain conditions) of the investigated specimen. An pretty unique characteristic of SEM images is their 3D appearance, thanks to the large depth of filed, that make them very similar to the images taken by human eyes.

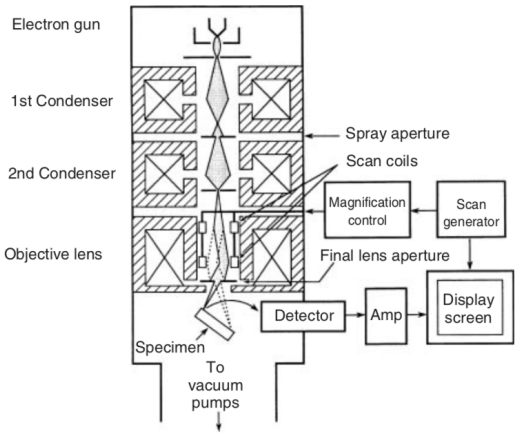

Figure 3.6: SEM instrumentation [27]

The basic principle of SEM (figure 3.7) consists of a creation of a focused electron beam by the emission from an electron source.
Typically, the energy of electrons is ranging between 0.1 eV and 30keV. After the emission and acceleration towards high energy, the electron beam is then focused by magnetic or electrostatic lenses. The electromagnetic coils act to reduce the crossover beam diameter and to focus it in a raster pattern.
The probe scanning is managed by a beam deflection system embedded within the objective lens. A rectangular raster is formed on the specimen surface since the deflection system moves the probe following a line and then displaces the probe to a position on the next line. A detector collects the signal of the electrons emitted from the surface of the sample.

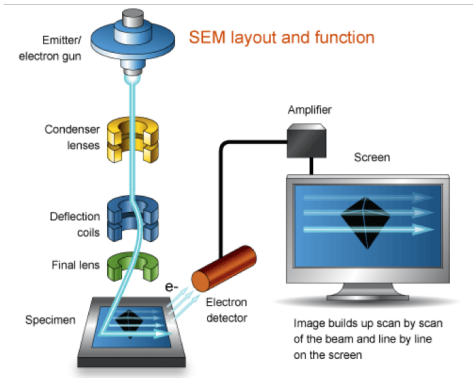

Figure 3.7: Basic principle of SEM

Different interaction can derive when a primary electrons beams imping on the surface of the sample (figure 3.8).

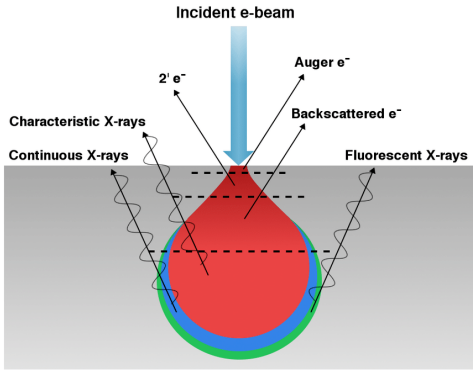

Figure 3.8: Interaction volume of an incident beam of electrons that produces a different effect at specific depths

Two different types of emitted electrons are detected in SEM:

- **backscattered electrons (BSEs)**: are electrons of the incident beam that emerge from larger interaction volume with an energy to the one of the primary beam. Backscattered electrons are a result of the elastic collision between the electron and atoms, which results in a change of the trajectory of electrons. The BSE images can provide different informations, such as both crystallography and compositional contrast. Their emission coefficient depends on the atomic number of atoms in the sample and also on the crystallographic orientation (channeling effect) as well as on the angle between the incident beam and the sample detail surface. BSE image shows high sensitivity to differences in atomic number since the higher Z, the brighter the materials appear in the image.
  The BSE detector is placed above the sample, concentrically to the electron beam in order to maximize the collection of the backscattered electron.

- **secondary electrons (SEs)**: are low energy electrons ($< 50eV$) that leave the surface of specimen (interaction thickness $< 10nm$). SEs are due to the inelastic interactions between the primary electron beam and the sample. Belonging to the sample atoms, they provide useful information about the topography of the sample surface.
  Historically, the most used device to detect SE was the Everhart-Thornley detector. It is composed of a scintillator inside a Faraday cage, which is positively charged and so attracts the SE. To increase the efficiency of secondary electrons, the detector is placed at the side of the electron chamber, in an angle. Nowadays, an additional SE detector is available and extensively used in the modern SEMs. It is the so called In-lens detector, placed along the column, above the objective lens of the SEM, collects the SEs thanks to an additional electrical field capable to attract the low-energy secondary electrons and to make them to move backwards along the column. Compared to the side-mounted ETD, the collection is isotropic and typically with an higher signal-to-noise ratio, making the In-Lens detector the preferred choice in many applications.

In the figure 3.9 is reported as an example, the SEM image obtained collected the SEs (on the left) and the BSE (on the right).

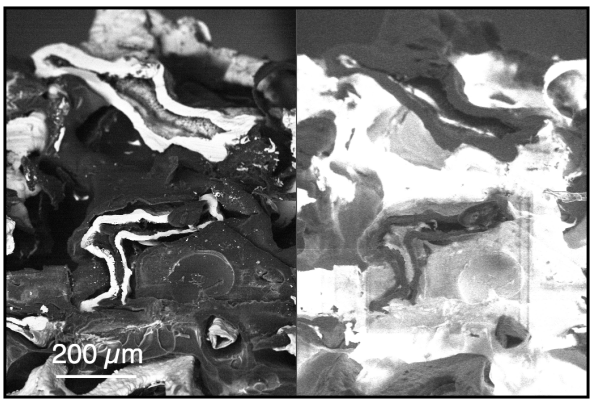

Figure 3.9: SEM image of graphene-PMMA matrix collected using the two different detectors: on the left SE, and on the right BSE

The interaction of the primary beam with the sample can also produce two different types of X-ray photon emission. A characteristic X-rays that possess a certain energies specific for each elements due to the electronic transition between atomic levels. The second type are continuum X-rays which form background and they are result from deceleration of the primary electron beam and. In the last case they will produce an homogeneous background that limit the minimum detectable signal, while characteristic X-rays spectrum can be used for compositional analysis.
Two different analysis techniques are possible. In energy dispersive spectroscopy the energy of the X-rays is used to produce a voltage pulse by means of suitable detectors. Pulses with similar intensities will be added together and will constitute the spectrum. In wavelength dispersive spectroscopy instead, each component of the spectrum is analysed individually. The analysed wavelength can be easily selected by diffraction from a known crystal. WDS allows to reach higher resolution but it is much slower. The dector for the X-ray used is Si(Li) detector. The base principle of this deterctor is the interaction of X-ray with a Si monocrystal doped with Li. The photons generate an electron-hole pairs that give a response of current proportional to the energy. Then, an impulse is measured and memorized in a multi channel analyzer that permits to obtain the spectrum. The working temperature is -200°C and the ultra vacuum is required. This type of detector is recently substitute with *Silicon Drift Detector* which is composed by a high pure Si and a Peltier system is used to cooled. The basic principle is the same for the other detector: X-ray hits the depletion region and the electron-hole pairs are generated. As a result an electrical signal can be detected [28].

3.3 Raman Spectroscopy

Raman spectroscopy is a non-invasive technique based on light scattering that it can be used to characterize the internal structure of molecules and crystal. Besides, it can also be useful in order to perform compositional analysis and to establish the degree of crystallinity of a sample.
More precisely Raman spectroscopy measures the vibrational motions of molecules, as well as infrared spectroscopy. However, while infrared spectroscopy is based on the absorption of photons, Raman spectroscopy exploits the Raman effect, a phenomenon of diffusion of light by atoms or molecules. When a monochromatic electromagnetic radiation impinge on an ideal system, it is mostly transmitted. One part of the light is diffused elastically, thus it has the same frequency as that incident wave, and in this case we speak of Rayleigh scattering. Another part instead is in-elastically diffused (Raman scattering). If the light diffused inelastically has less energy than that incident beam then one speaks of Stokes-Raman scattering, in the opposite case, if it has more energy, one speaks of anti-Stokes-Raman scattering. On the other hand in elastic scattering there is no energy exchange between the incident photon and the atom or molecule with which it collides, instead a transfer of energy between the photon and the vibrational or rotational degrees of the molecule occurs.
Typically the intensity of the diffused radiation is lower than a factor 10^3 compared to the intensity of the incident radiation, and, in turn, the radiation that undergoes Raman scattering is approximately 103 times less intense than the Rayleigh diffusion ($I_{Raman} = 10^{-3} I_{Rayleigh} = 10^{-6} I_{incident}$). For this reason, although the phenomenon of Raman diffusion had been experimentally observed for the first time in 1928 by the Indian physicists Raman and Krishnan, physicists began to be interested in it in depth only 30 years later with the use of the first laser, as they are high intensity monochromatic light sources. Figure 3.10 shows the components of a typical experimental set-up for Raman spectroscopy. It consists of:

- **Laser**: it is the source of the light radiation to be sent to the sample. As already explained, lasers producing monochromatic and high intensity radiation necessary to be able to observe sufficient Raman diffusion events. Furthermore, lasers are a source of polarized light, so it is possible to observe the depolarization factor, a phenomenon associated with the change in the direction of polarization of light after Raman scattering [29].

- **Sample**: the diffused light is distributed in all directions. Two geometries are mostly used: one, in which the diffused light is observed at 90^o with respect to the direction of the incident beam, is mainly used for liquid samples. The other is used for solid samples and the light coming back from the sample (angle 180^o with respect to the direction of the incident beam). In general, the intensity of the retro-diffused light is greater than the first configuration.

- **Filter**: the light diffused by the sample contains both the Rayleigh and the Raman components. The first one must be eliminated because it is too intense compared to the second, so the filter has be designed in order to cut only the light with the same frequency of the incident beam. For this reason Notch filters are used. Obviously each type of laser must have a Notch filter designed specifically for its wavelength.

- **Spectrometer**: the part of light selected by the filter must be resolved in frequency before its collection. This spectral dispersion is made possible by a diffraction grating that diffracts each wavelength of the incident light at different angles.

- **Detector**: CCDs (Charge Coupled Devices) are generally used as detectors characterized by low noise and the possibility of acquiring 2D images.

In the molecules, the interaction of light is mainly determined by the energy levels of the degrees of freedom inside the molecule. This latter is associated with the movement of electron or atoms inside

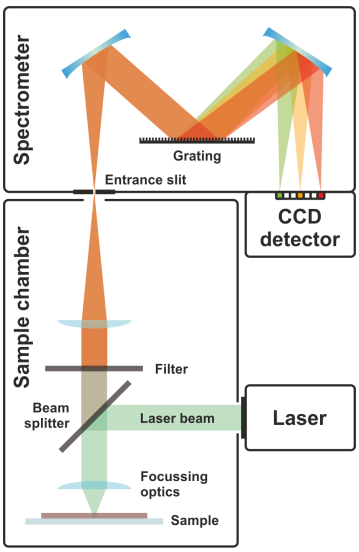

Figure 3.10: Raman experimental setup

the molecule such as vibrational, rotational or translational energy levels. In molecular spectroscopy, in order to visualize the energy levels, it is useful to use the Jablonski diagram in which is presented the energy vs the normal mode coordinate. All energy levels (electronic and vibrational) are shown by horizontal line. Moreover, a thin line represented the motional states for each electronic state. The transition between state instead is shown by arrows.
This technique is based on the Raman effect in which light of a known frequency and polarization is scattered from a sample. Then, the impinging light is scattered into different components depending on the energy of the incident photon. Raman scattering is a typical inelastic scattering; in fact, the scattered photon is at different energy of the incident (figure 3.11):

- **Stokes process** if the scattering photon (E_S) possess less energy than the incident one (E_L). The molecule is excited to a higher energy level.
- **anti-Stokes process** if the scattered photon has more energy concerning the incident one. The molecule has relaxed from an excited vibrational state to its ground state.

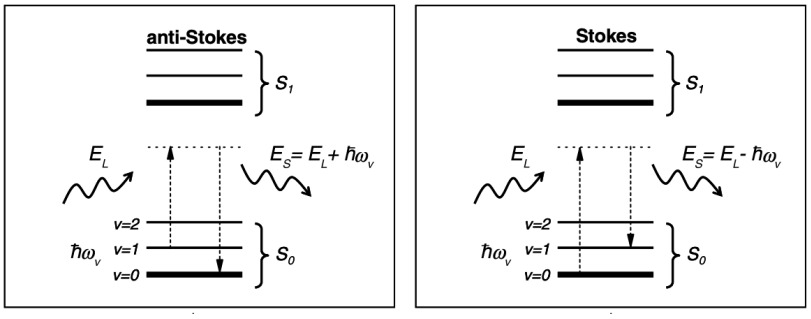

Figure 3.11: Jablonski diagram of anti-Stokes and Stokes Raman process

During the scattering events, the energy lost by the photons is called *Raman shift* and it is defined as $\Delta E_R = E_L - E_S$. Therefore it is positive for Stokes process and negative for anti-Stokes one.
Raman spectrum, instead, correspond to the wavelength (or energy) vs. the scattered intensity at fixed

incident wavelength. Peaks in the Raman spectrum correspond to vibrational modes of the molecule.

3.3.1 Graphene Raman spectra

Raman spectroscopy has played an historically important role in the study and characterization of different carbon allotropes, including graphene. The graphene and graphite Raman spectra have a relatively simple structure, characterized by the presence of three peaks: the G band, the D band (which appears only in the case in which the graphene has defects) and the 2D band. Through the study of Raman spectra of graphene, it is possible to trace the number of layers of which it is composed since the position, intensity, and width of the peaks depends on it. They can also depend on other factors such as the emission wavelength of the laser used or the stress conditions to which the sample is subjected. Let us now analyze the origin and characteristics of the various peaks:

- **G peak**: This peak is positioned at about $1585cm^{-1}$ in the spectrum. This is due to the lattice vibrations in the plane of the $C-C$ bond in the sp2 configuration. In general, all spectra are dominated by this type of reticular vibration: peaks due to vibrations in sp3 configuration are observed only in diamond using UV rays as a source of photons [37]. Because of the interactions between atomic planes, the position of the G peak is sensitive to the number of layers from which the sample is composed, so by determining its position accurately it is possible to trace the number of layers of graphite. Increasing the number of layers, the peak moves towards lower energies. However the position of the peak is sensitive to the number of graphene layers only if these are few; in fact for a consisting of 10 layers, the position and shape of the G peak can no longer be distinguished from that of graphite. Neither the position nor the shape of the peak depends on the frequency of the laser used, however they depend on other factors such as the stress applied to the sample, the doping levels of graphene, or the temperature. In particular, the frequency at which the peak is located depends on the hydrostatic pressure acting on the sample and an uniaxial stress applied to the sample can divide it into two: a G^- peak relative to the atomic motion along the direction of elongation, and a peak G^+ relative to the motion in a direction perpendicular to the elongation. Furthermore, as the temperature increases, the peak moves towards lower energies.

- **D peak**: This peak is related to the disorder or defects in the structure of graphene. It is positioned between $1250-1400cm^{-1}$ and is related to the breath modes of the hexagonal carbon rings. Using an energy from the laser of the order of $E = 2.41eV$, the peak is positioned at around $1350cm^{-1}$, but the position of the peak changes as the laser energy changes. Furthermore, its dispersion varies with the carbon nanostructure under examination and depends on the number of graphene layers.

- **2D peak**: It corresponds to the second order of the D band and it comes from the vibrational process of the two phonon lattice with opposite moment, located in the highest area of the optical branch, near the cone of the first Brillouin area. Its position depends on the energy of the laser: again, for $E = 2.41eV$ it is found at $2700cm^{-1}$. Both the position and the structure of this peak strongly depend on the investigated carbon nanostructure and the number of layers, for this reason this band is used to determine the number of layers of which a graphene sample is composed. In particular, for graphene monolayer, the 2D band is composed of a single Lorentzian peak, while for graphene bilayer it is composed already of 4 Lorentzian peaks. For three layers the 2D band structure is very complicated: it is composed of 15 peaks very close in frequency, so that generally only 6 of these are distinguishable.

As already mentioned, it is possible to determine the number of graphene layers in the sample through the ratio of the intensities of the 2D and G peak, even if only if they are less than five. In

fact, the G and 2D peaks for structures composed of ten or more graphene layers are indistinguishable from those of graphite. In any case, the I_{2D}/I_G ratio is extremely sensitive to the number of graphene layers: for a single layer it is about 4 and decreases rapidly as the number of layers increases.

3.4 X-Ray Diffraction Analysis

Diffraction effects are observed when electromagnetic radiation impinges on periodic structures with geometrical variations on the length scale of the wavelength of the radiation. The interatomic distances in crystals is about 0.15– 0.4 nm, which correspond in the electromagnetic spectrum with the wavelength of X-rays having photon energies between 3 and 8 keV. Accordingly, phenomena like constructive and destructive interference should become observable when crystalline and molecular structures are exposed to X-rays.
X-Ray Diffraction Analysis (XRD) is a non-destructive technique based on X-rays, electromagnetic waves in which the typical energy range is 0.1 to 100 keV. This characterization is based on constructive interference of monochromatic X-rays and a crystalline sample. The X-rays are generated by a cathode ray tube, filtered to produce monochromatic radiation, collimated to concentrate, and directed toward the sample. The interaction of the incident rays with the sample produces constructive interference (and a diffracted ray) when conditions satisfy Bragg's Law. This law relates the wavelength of electromagnetic radiation to the diffraction angle and the lattice spacing in a crystalline sample. The characteristic X-ray diffraction pattern generated in a typical XRD analysis provides a unique "fingerprint" of the crystals present in the sample. When properly interpreted, by comparison with standard reference patterns and measurements, this fingerprint allows identification of the crystalline form. X-ray diffraction is useful for evaluating minerals, polymers, corrosion products, and unknown materials. This technique is used as well in order to obtain information about roughness, density and thickness of single or multi-layers film. In more details, the basic physical principle of this technique is the coherent elastic scattering of the radiation from ordered lattice planes. As we mentioned before, **the Bragg's law** describe the basis of the diffraction process (figure 3.12):

$$2dsin(\theta) = n\lambda \tag{3.6}$$

in which θ is the incident angle, λ is the wavelength of the incoming electromagnetic wave, and d is the distance between two different lattice planes of the same orientation.

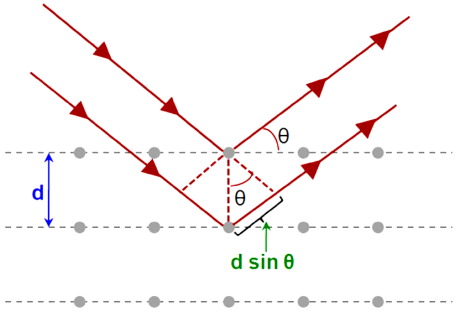

Figure 3.12: Condition of the Bragg's law

A crystal is made up of the same repeating units, and in this way, constructive interference is formed only in specific directions. Moreover, it will depend on the wavelength of the primary beam and the periodicity of the crystal.
In order to describe the diffraction, the reciprocal space is considered. In particular, the reciprocal space is represented by the notation:

$$G_{hkl} = ha' + kb' + lc' \tag{3.7}$$

where h, k, l are Miller indexes, and they represent a plane in the crystal with the intercepts $1/h', 1/k'$, and $1/l'$ respectively with the axes a, b and c. Another method to describe the diffraction in the

reciprocal space is to consider the Laue condition:

$$qa = 2\pi hqb = 2\pi kqc = 2\pi l \tag{3.8}$$

where q is the scattering vector defined as the difference between the incoming and outgoing wave vectors. The Laue conditions guarantee if the diffraction that place and this can be obtained by substitute into the scattering vector formula:

$$q = ha' + kb' + lc' \tag{3.9}$$

Thus the Bragg condition is satisfied when q intersects the reciprocal point at the position defined by the general lattice vector G_{hkl}:

$$q_B = 2\pi|G_{hkl}| \tag{3.10}$$

Thanks to the XRD techinique it is possible to determine the crystal structure since the position and the intensity of the diffraction peaks correspond to the position of the atom inside the lattice structure.
In the ideal case of an infinite crystal, peaks will generate a distribution that follows the Dirac Delta function, where all the points are equal to zero except for zero. When it comes to a real crystal with a definite dimension, it's possible to notice the broadening of Bragg's peaks. The broadening of the peaks is due to the deformations of the crystal as well. As a first approximation, the formula that relates the average size of sub-micrometer crystallite in a solid to the broadening of a peak in a diffraction pattern is well described by the Scherrer equation that was published in 1918. This equation can be written as:

$$L_{hkl} = \frac{K\lambda}{Wcos\theta_B} \tag{3.11}$$

where L_{hkl} is the mean size of the ordered crystalline domains, which may be smaller or equal to the grain size; K is a dimensionless shape factor, with a value close to unity. Normally, the shape factor has a value of 0,9, but it may vary with the actual shape of the crystallite; λ is the X-ray wavelength; W is the line broadening at half the maximum intensity (FWHM), after subtracting the instrumental line broadening, in radians. This quantity is also sometimes denoted as (2θ); θ is the Bragg angle.
The Scherrer equation is limited to nano scale crystallite where the grains dimension do not exceed 1000-2000 Angstrom. When the microstructure shows bigger grains it is necessary to use different and more precise techniques. For a single crystal, the reciprocal lattice is formed by a set of points, while in a polycrystalline material, where there are different grains with different orientations, the reciprocal lattice is formed by a set of different concentric rings so the radius is related to the modulus of the lattice vector. In this work, the measurements were carried out by using a Smartlab Rigaku diffractometer, (figure 3.13) is composed of rotating copper anode, sample stage able to move in x-y plane and a point detector.
Firstly, the electrons are produced by the thermionic effect from the tungsten filament (cathode) which is heated by the electrical current. Electrons hit the rotating anode, and in this way, the X-rays are emitted. The rotating anode permits to disperse the heat of the incoming cathode and so long scan at high intensity can be performed. The incident optics is constituted by a paraboloidal synthetic multilayer mirror coupled with a Germanium channel-cut crystal. It serves to monochrome and collimate the divergent beam generated from the X-ray source into a parallel beam, and it is composed by a width-limiting slit which restricts the width of the sample area irradiated by the X-rays. The receiving optics is characterized by another Ge channel-cut crystal called analyzer, a receiving soller slit and a detector. The detector is a scintillation counter, and it is positioned on the receiving arm of the diffractometer which can move both in the out-of-plane (z) and in-plane (x-y) directions.

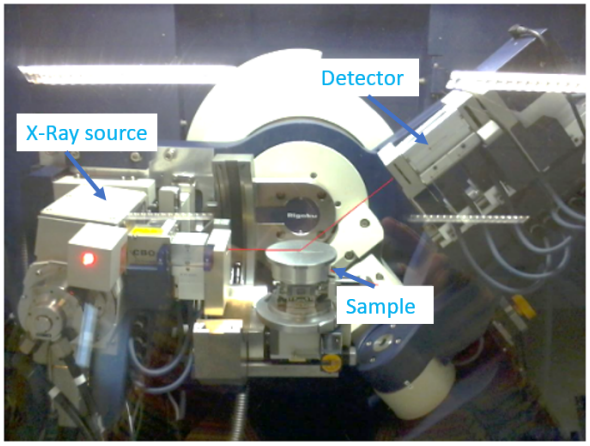

Figure 3.13: Experimental setup of X-rays diffractometer

In this case, the characteristic wavelength of the X-ray source is well known and it is λ equal to 1,5405 Angstrom, related to an energy of 8048,3 eV. Thanks to the rotating anode, the impact surface where the electrons emitted by the cathode are sent, is increased and the photons flux is greater of several order of magnitude. The data collected will generate a curve that is called diffractogram, where the number of detected photons are shown as a function of time and angle 2θ.

4. Process

In this chapter, the steps and the related problems encountered during the process are detailed in the paragraph below. The synthesis of GF are reported in figure 4.1 in which two different structures of Nickel foam are taken into account. Moreover, the main steps in order to obtain PDMS/Graphene foam are:

- *Chose the Nickel Foam as a template for the growth of GFs*: the Nickel sponge is constituted by a porous structure with an interconnected 3D scaffold of Nickel.
- *Preparation of Nickel Foam*: the Ni-foam was cleaned in an ultrasonic bath, using a solution of HCl (concentration 3.7 wt.%) in order to remove the surface oxide layer, then in deionized water to remove residual HCl and finally in acetone to remove organic impurities. This passage was carried out for two minutes per each solution.
- *Deposition of Graphene by CVD*: the sample was placed inside the furnace where the deposition takes place, and annealed at 1000°C under H_2 flux. CVD was carried out by combining different gases such as CH_4, and H_2. Then the sample was left inside the chamber to cool it. Due to the thermal expansion of Nickel and graphene, ripples and wrinkles are formed which guarantee a better adhesion of the following polymer integration inside the GFs.
- *Infiltration of Poly-methyl methacrylate (PMMA)*: PMMA was infiltrated into the GFs to fill the holes by a polymer matrix.
- *Ni skeleton etching*: the foam was left several days in a solution of $4,5\%$ $FeCl_3$ at 80 $°C$. , to remove Ni, then it was gently washed in deionised water and left one day in a solution of $10\% HCl$ to remove the traces of $FeCl_3$.
- *Infiltration of Poly-dimethylsiloxane (PDMS)*: the space released by Ni etching was filled by PDMS in order to give flexibility and resistance to the structure. The polymer is formed by two parts: one is the base, and the other is the curing agent. Firstly, the two agents were mixed with a mass ratio of 5:1 (base: curing agent) and then the sample was immersed in the PDMS. A vacuum pump performed the infiltration of the polymer for 30 minutes, then the sample was post-backed at 60 $°C$ for 1 hour, in order to carry out the thermal curing of PDMS.
- *Removal of PMMA*: PMMA matrix was dissolved in acetone and then blow-dried to obtain a monolithic interconnected 3D graphene network. After removal, the GFs became thinner than the original thickness of the Nickel foam.

4.1 Choice of the metal substrate

Among different techniques avaible to produce graphene, CVD on a transition metal substrate becomes the most employed. The main reason is that CVD method permits to grow high quality graphene

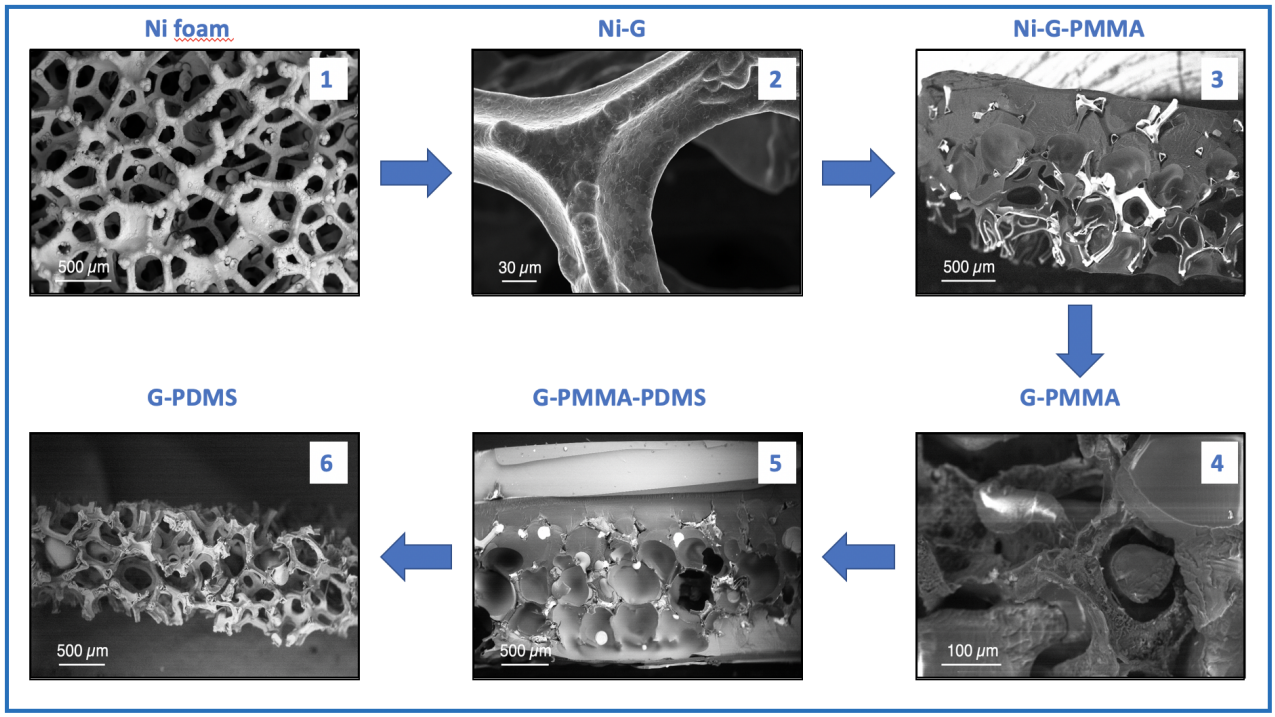

(a) CNR Ni-foam

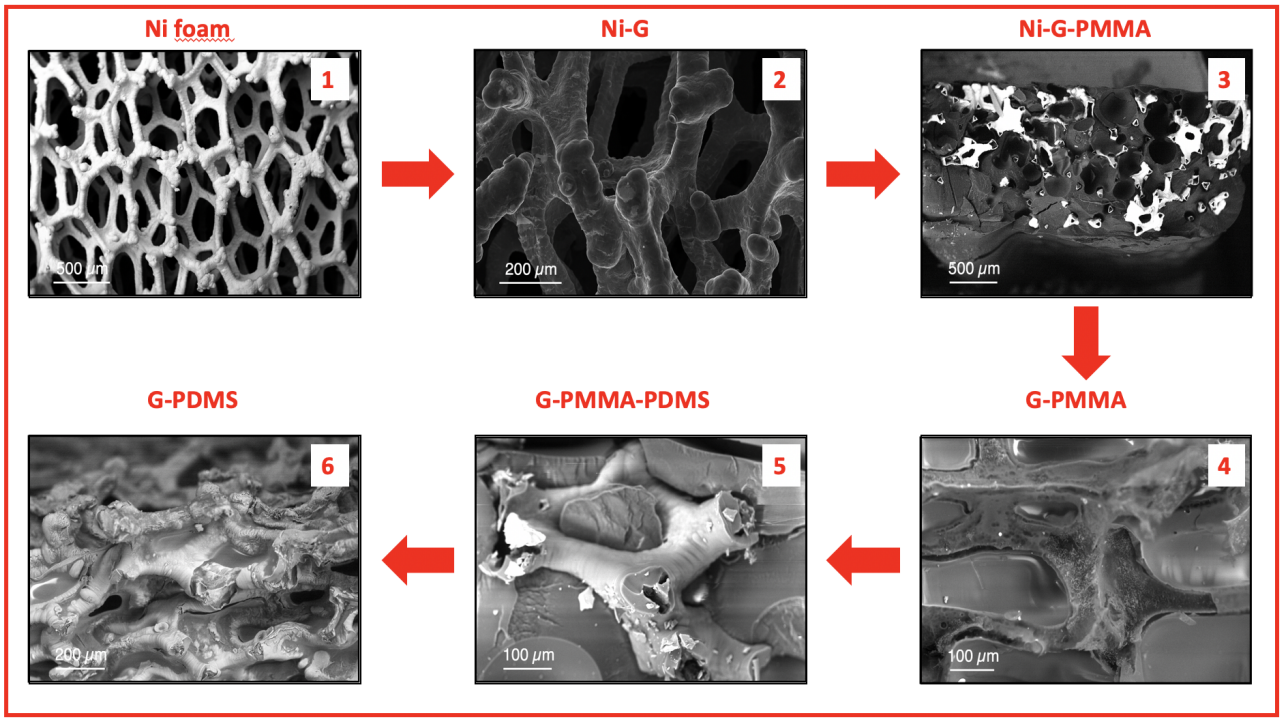

(b) Politecnico di Torino Ni-foam

Figure 4.1: SEM images of each step: 1) pristine Ni template, 2) after G deposition, 3) after PMMA infiltration, 4) after Ni etching, 5) PDMS infiltration, 6) after PMMA removal

film, and it is also possible to control graphene nucleation in a large-area. Different factors affect the final quality of deposition such as growth temperature and time, hydrocarbon concentration (for example CH_4), hydrocarbon pressure, cooling rate and finally solubility of carbon atoms in the metal substrate.
The choice of an adequate metal substrate is important for two main reasons [30]:

- it works as a catalyst in order to decrease the energy barrier during the deposition of graphene;
- it determines the graphene deposition mechanism that, in turn, affects the quality of the final product.

Typically Nickel and Copper are the most used catalyst substrates, but graphene growth mechanisms and the graphene thickness are entirely different, figure 4.2. Firstly, these peculiarities ascribe to the different solubility of carbon atom into the two metallic substrate. Which is $<$ 0,001 atomic % for Cu and $>$ 0.1 atomic % for Ni. [31]. As a result, a *multilayer* G growth occurs on Ni substrate, whereas a *uniform monolayer* G grows on Cu substrate
Cu is considered the best candidate since it is less expensive than Nickel, it possesses a well-controlled surface but it shows a lower carbon solubility and catalytic effect than Ni. The growth of graphene on Cu substrate is characterized by three main steps [32]:

- adsorption and decomposition: carbon is separated from the precursor and deposited on the copper surface;
- diffusion and desorption: due to the low solubility, carbon atoms diffuse on the surface;
- nucleation and growth: a nucleation site is formed, defects act as a center upon which additional carbon atoms are deposited as the crystal grows.

The CVD graphene growth mechanism on Cu substrate is a surface deposition. Carbon atoms are directly deposited on the catalyst surface without segregation. This implies that, after the deposition of the first graphene monolayer, the copper surface is entirely covered. Therefore, no catalyst is exposed preventing the chemical reaction and the growth. Regardless the hydrocarbon concentration and the deposition time, only a small amount of carbon is dissolved in Cu leading a uniform monolayer growth.
Concerning, Ni substrate, the growth mechanism is different. Ni possesses a lattice structure similar to the densely packed hexagonal lattice of graphene, and they also have a similar lattice constant. For these reasons, Ni surface can serve as an excellent lattice-matched substrate for CVD graphene.
The graphene growth mechanism on Ni consists in a carbon atom segregation and precipitation processes due to the following phenomena [33]:

- carbon diffusivity: at high temperature, carbon atoms are catalytically produced from methane decomposition that occurs on Ni surface. Ni grain boundary acts as a nucleation site, and besides, bigger Ni crystal grain size more the graphene flakes are extended;
- carbon precipitation: during the cooling step, precipitation of carbon atoms on Ni surface occurs due to the supersaturation of diluted carbon in Ni. During this phase, several graphene layers are formed. The final number of layers deposited depends on the cooling velocity: indeed, the decrease of velocity permits to deposit more layers. The dimension of the graphene crystal is inversely proportional to the nucleation site density. This latter can be decreased by increasing the hydrogen/methane ratio and by raising the temperature during the annealing and deposition. A long-time is required in order to deposit graphene layer with large flakes.

In this study, Nickel foam is chosen as the substrate to deposit multilayers of graphene, since it guarantees the fabrication of a free-standing structure. Indeed, monolayer deposited on Cu substrate

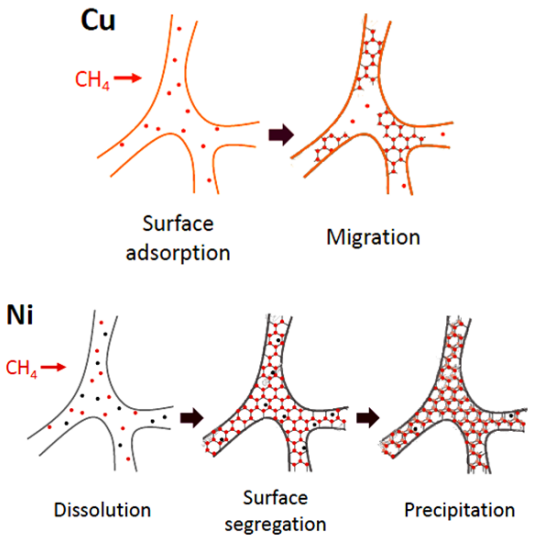

Figure 4.2: Two different graphene growth mechanism on Ni substrate and Cu template

collapsed after the metal etching, preventing to maintain the 3D foam structure. Two different templates of Ni foam has been used, one provided by CNR-Bologna and one provided by Politecnico di Torino. Several techniques have been used: SEM to characterize the graphene foam morphology, Raman spectroscopy to detect the graphene quality and XRD to estimate the number of graphene layers.

4.1.1 Ni-Foam CNR

The main properties of Ni-foam provided by CNR-Bologna are:

NI003852/15	
Thickness	1.6 mm
Bulk density	0.45 g/cm^3
Porosity	95 %
Porosity/cm	20
Purity	99.5 %
Net weight	132 g

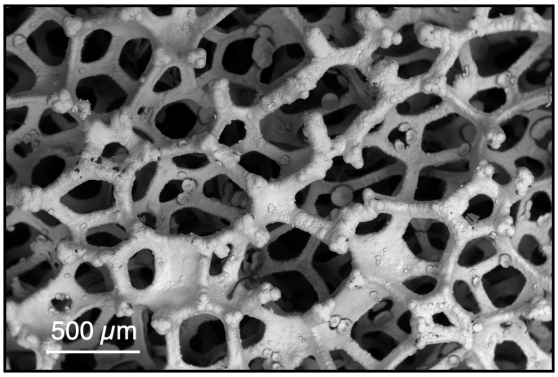

(a) Ni-foam skeleton

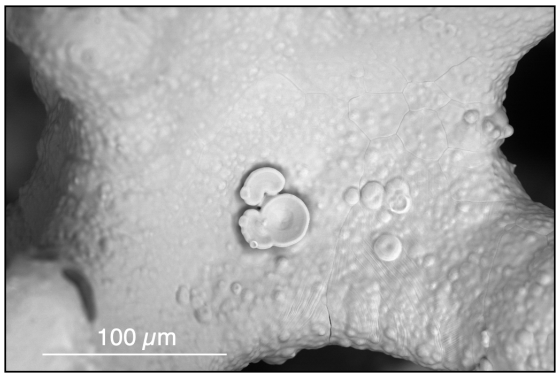

(b) Detail of the Ni surface

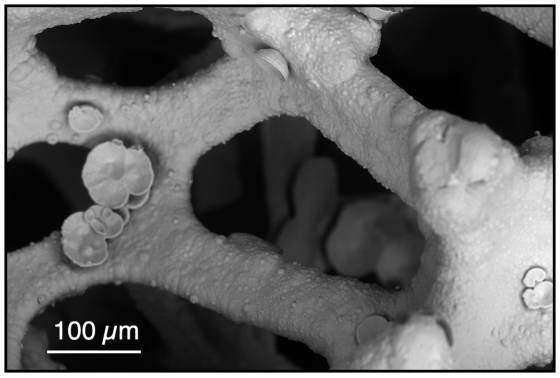

(c) Detail of Ni surface with a magnification of 500x

Figure 4.3: SEM images of Ni-Foam CNR

4.1.2 Ni-Foam Politecnico di Torino

Ni-Foam analyzed in Politecnico di Torino possesses the following properties:

NI003840/1	
Thickness	0.9 mm
Bulk density	0.62 g/cm^3
Porosity	93 %
Porosity/cm	20
Purity	99.5 %
Net weight	55.8 g

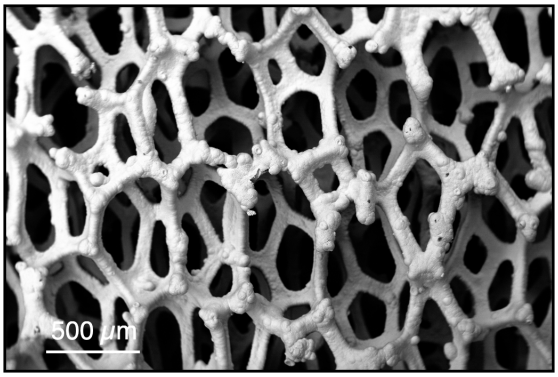

(a) Ni-foam skeleton

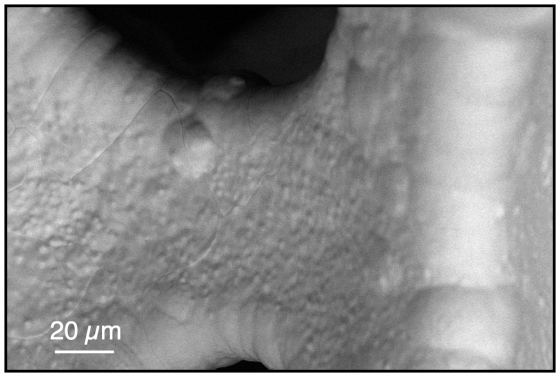

(b) Detail of the Ni surface

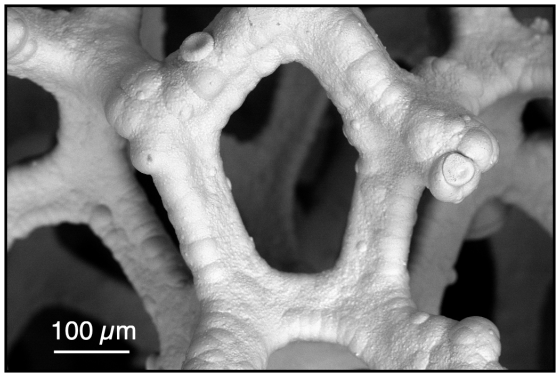

(c) Detail of Ni surface with a magnification of 500x

Figure 4.4: SEM images of Ni-Foam Politecnico di Torino

4.1.3 Morphological comparison between the two Ni-Foams

Figures, 4.3a and 4.4a report the SEM images collected for the Ni foam provided by CNR-Bologna and Politecnico di Torino, respectively, showing that the skeletons of the two Ni-foams are different. The skeleton of CNR Ni-Foam is characterized by quite circular section; differently, the one of Politecnico di Torino possesses a hollow branches and stretched circular pores. SEM analysis permits to estimate the distribution of diameters of porous for each Ni-foam:

- **CNR foam**: dia.= from ~ 120 μm to ~ 380 μm
- **Politecnico di Torino foam**: dia.= from ~ 160 μm to ~ 450 μm

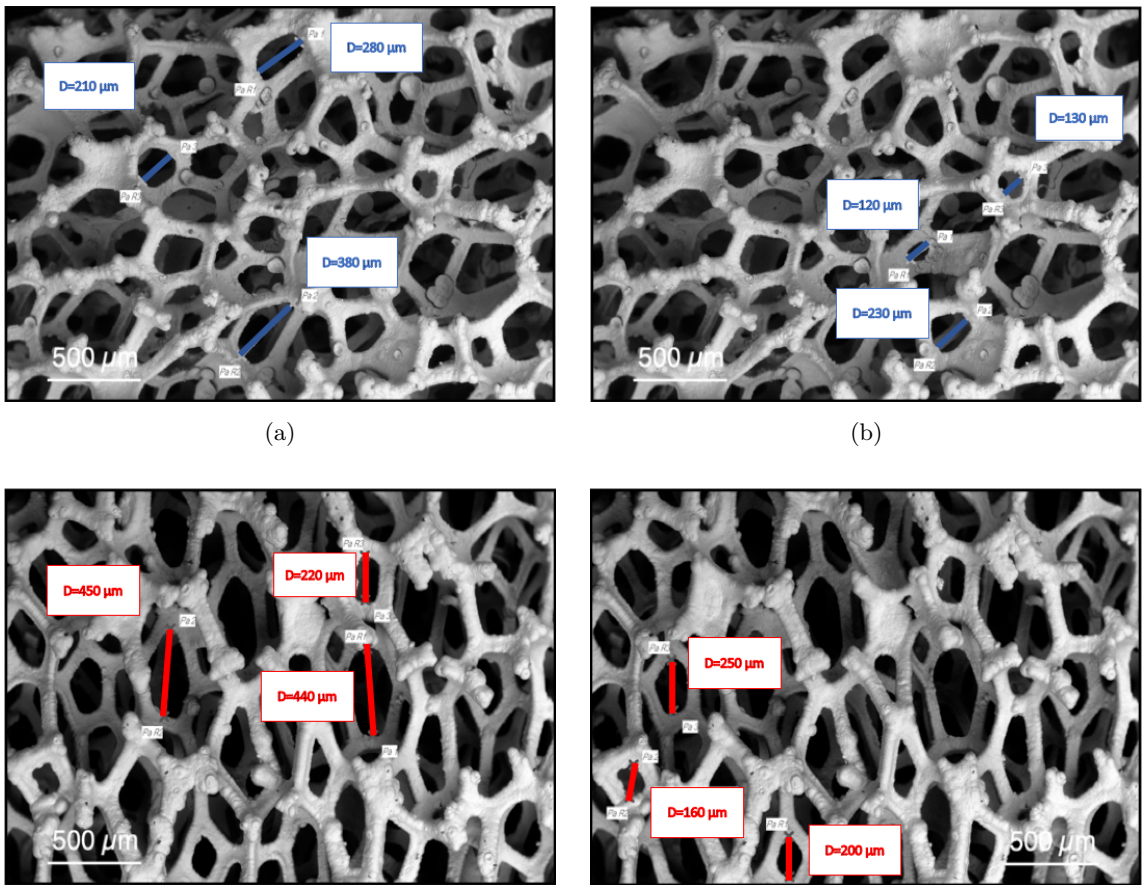

Figure 4.5: SEM images of Ni-Foam to establish the diameter of porosity for each Ni template. Figure a) and b) correspond to CNR foam, instead c) and d) are the Politecnico di Torino foam

SEM images collected using a higher magnification (figure 4.3c and 4.4b) reveal that both foams possess some superficial rugosity and different particle derive, possibly, from contamination. These can be eliminate with by pre-cleaning of the foam before the CVD.

4.2 Graphene multilayer thickness

In this study, deposition time and flux concentration have been tuned to obtain three different thickness of graphene multilayer:

- **Thin film**: flux 10 sccm of CH_4 and deposition time of 5 minutes.
- **Medium film**: flux 50 sccm of CH_4 and deposition time of 5 minutes.
- **Thick film**: flux 50 sccm of CH_4 and deposition time of 10 minutes.

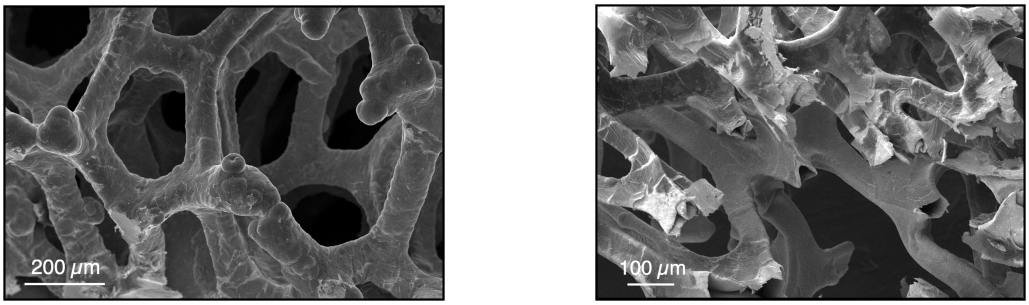

(a) Politecnico di Torino foam (b) CNR foam

Figure 4.6: Examples of SEM images collected on the two different template after graphene CVD

In figure 4.7 a detail of SEM images of the sample $\#SGF19007$ is reported. From the images, it is possible to clearly identify the graphene layer deposited on the Ni surface.

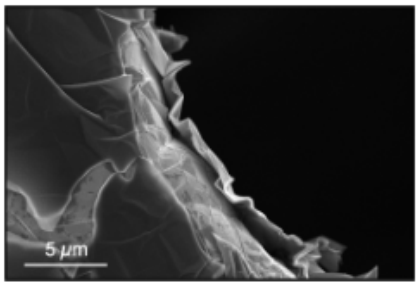

(a) SEM image of sample $\#SGF19007$ after graphene deposition

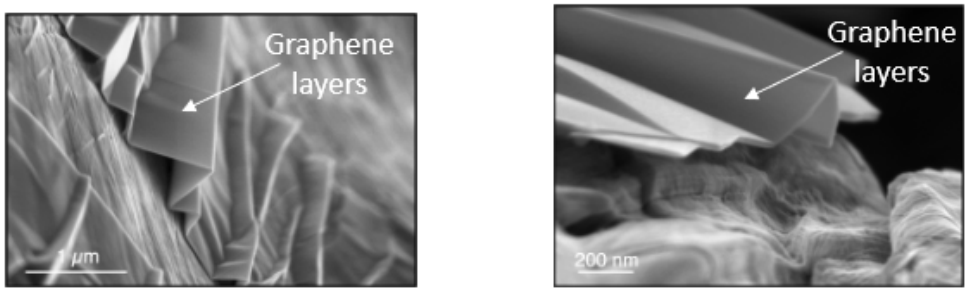

(b) (c)

Figure 4.7: SEM images of details of graphene layers formed during deposition on Ni template. From the image wrinklesd is obrserved after the graphene deposition.

4.3 Graphene Raman Spectroscopy

The Raman technique allows to detect the quality of graphene layers deposited by CVD, as Raman spectroscopy reflects changes in the electronic bands of the material. For this reason the Raman spectrun of a graphene membrane can be used as its fingerprint, identifing the number of layers and the disorder in its plane, with influences on its properties.
In order to understand the Raman spectra of graphene, it is useful to understand the phonon dispersion of this material. As mentioned before, the unit cell of graphene is composed by two carbon atoms, so six phonon dispersion bands can be found: three are acoustic branches and three optical phonon branches.
For one acoustic and one optical branch the atomic vibrations are perpendicular to the graphene plane, *out-of-plane phonon mode*. For the remaining two acoustic and optical branches the vibrations are *in-plane*. The phonon modes can be classified into longitudinal and transverse, depending on the direction of vibration if it is parallel or perpendicular to the direction defined by the two carbon atoms inside the unit cell [34].

The Raman spectra of graphene show two characteristic peaks: the **G peak** at $\sim 1580\ cm^{-1}$, and the **2D peak** at $\sim 2700\ cm^{-1}$. They are due to the *in-plane* optical vibrations and the second-order zone boundary phonon vibrations respectively. An additional peak located at $\sim 1350\ cm^{-1}$, called **D peak**, is detected in defective graphene and corresponds to the first-order zone boundary phonon vibrations. Moreover, the number of layer forming the graphene membrane can be derived by the shape, position and width of the 2D peak, combined with the value of the ratio between the intensities of the 2D peak with respect to that of G peak.
An increasing number of layers correspond to a shift of the 2D peak toward higher wavenumbers and to an increase of 2D peak width and a decrease of the ratio between the 2D and G peak intensities.

Another important parameter is the intensity ratio between the D and G peak, that allows the evaluation of the disorder degree in the graphene membrane due to ripples, edges, charged impurities and domain boundaries.

Raman analysis was performed by means of a Renishaw InVia Reflex micro-Raman spectrometer (Renishaw plc, Wotton-under-Edge, UK), equipped with a cooled CCD camera. A laser diode source (λ_{laser}=514.5 nm) was used with 5 mW power, and sample inspection occurred through a microscope objective (50X), with backscattering light collection.

Figure 4.8 shows the Raman spectra measured in two region of the sample $\#SGF19005$. In region A the defect-related D peak is not detected, demonstrating that in this region the graphene grown by CVD on Ni has a high crystalline quality. The shape of 2D peak with the ratio of 2D and G peak intensities lower than 1 show that it is a multilayer graphene. The spectrum of region B exhibits a D peak and a shape of 2D peak typical of graphite, so this region has a larger number of graphene sheets. In fact, the 2D peak is formed by two components, roughly 1/4 and 1/2 the height of G peak, respectively, which is typical of bulk graphite [35].

Figure 4.9 reports the Raman spectra measured in two regions of the sample $\#SGF19006$. The presence of the D peak indicates that the 3D foam is defective, while the shape and intensity ratio of 2D and G peaks proves that the foam has a multilayers graphene structure.

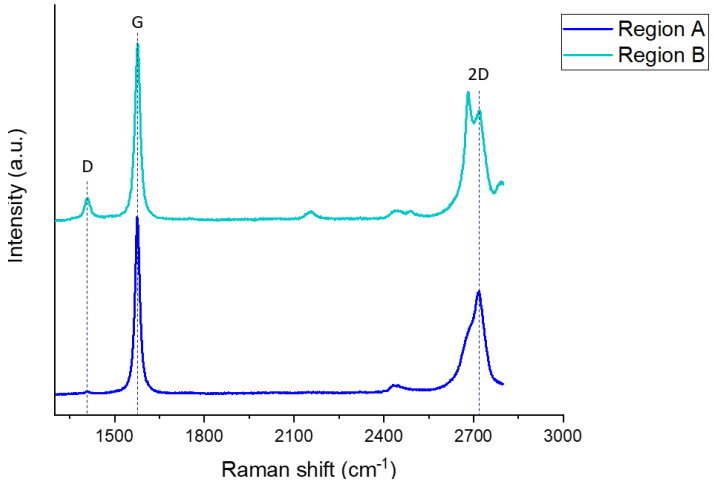

Figure 4.8: Raman spectrum of the sample $\#SGF19005$ collected from two different regions

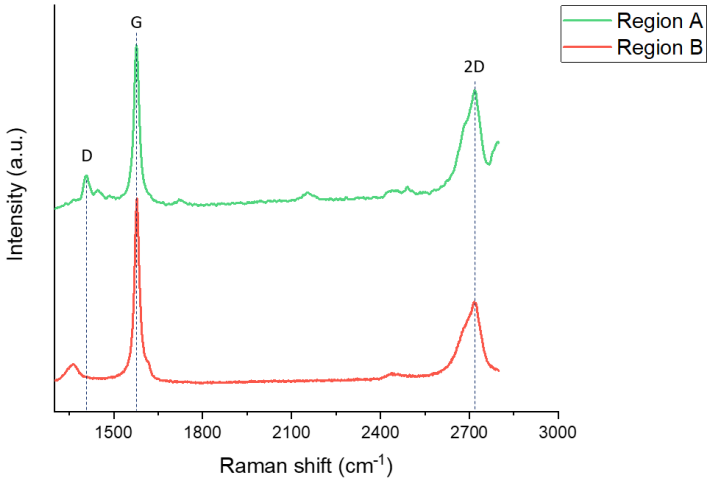

Figure 4.9: Raman spectrum of the sample $\#SGF19006$ measured consider two region of the sample

The Raman spectra of the sample $\#SGF19010$ are reported in figure 4.10 and show that also this foam is formed by a multilayer graphene structure. In particular, the purple curve (region C) is a characteristic Raman spectrum of PMMA, thus meaning that some PMMA residuals are left on the foam, not completely removed in some regions. In general, fewer defects, multi- or few-layers and the low intersheet junction contact resistance guarantee a high electrical conductivity of the 3D graphene foams. The presence of PMMA residuals in some regions can lower the graphene conductivity.

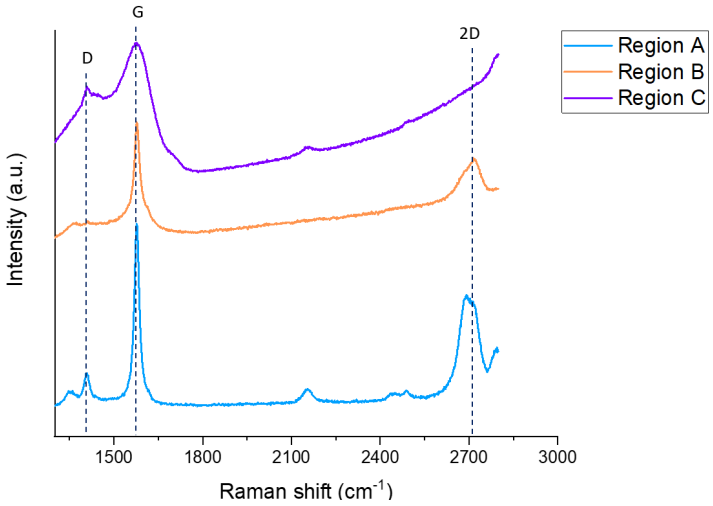

Figure 4.10: Raman spectrum of the sample $\#SGF19010$ measured consider three region of the sample

The relevant data obtained from the spectra are summarized in the table below.

	SGF19005		**SGF19006**		**SGF19010**
	A	B	A	B	A
D/G Intensity ratio	0,03	0,13	0,16	0,14	0,23
2D/G Intensity ratio	0,6	0,6	0,75	0,46	0,6

4.4 XRD analysis

After the CVD process samples have been characterized by XRD, a non-destructible technique allowing the foam to be totally probe.

Figure 4.11 shows the long 2θ scans performed on two samples, $\#SGF19010$ and $\#SGF19005$, collected after the CVD process and at the end of the G-PDMS foam fabrication. Bragg peaks coming from Ni crystal skeleton are well observable on both the samples after the graphene CVD. They disappear after the Ni etching, however, new Bragg peaks appear in sample $\#SGF19005$ which can be attributed to nickel oxide. This latter could be formed during the fabrication of G-PDMS foam, which steps are, as described later, PMMA infiltration, Ni etching, PDMS infiltration and PMMA removal.

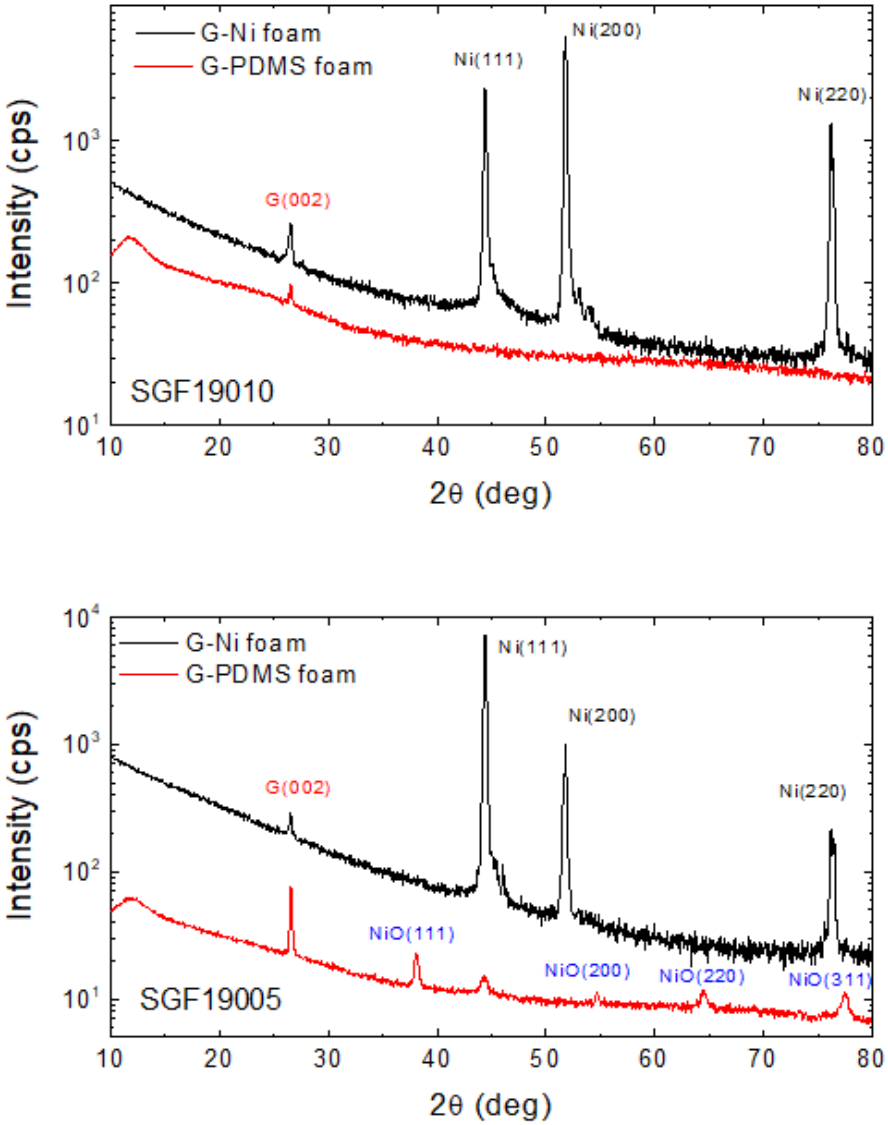

Figure 4.11: XRD (2θ scans) patterns collected on $\#SGF19010$ and $\#SGF19005$, after graphene CVD (black curves) and after the PMMA infiltration, Ni etching, PDMS infiltration and PMMA removal (red curves).

XRD technique has been used to estimate the number of graphene monolayers after CVD, by analysing the Bragg peak coming from the (002) plane of graphite crystal structure, that corresponds to the repetition of the graphene layers. The full width at half maximum (W) of the diffracted peaks is correlated with the coherent length L along the graphene repetition according to the Scherrer law:

$$L = \frac{K\lambda}{W cos\theta_B} \tag{4.1}$$

where K is a constant generally equal to 0.9 and θ_B is the angle position of the Bragg reflection and λ is the x-ray wavelength. In first approximation L is the size of the graphene multilayer.
To do that, specular scans with an acceptance of 0.03° have been collected around the G(002) peak and reported in figure 4.12.

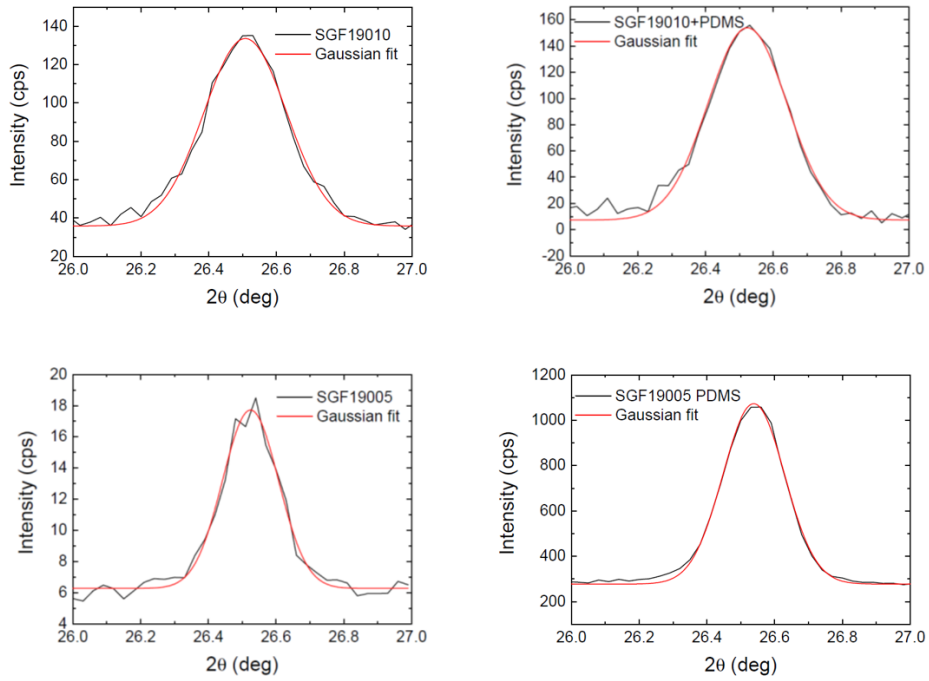

Figure 4.12: XRD specular scans collected on samples $\#SGF19010$ and $\#SGF19005$. Red lines are the fitting curves.

Experimental curves have been fitted using Gaussian function:

$$y(\theta) = y_0 + Ae^{\frac{(\theta-\theta_B)^2}{2w^2}} \tag{4.2}$$

where y_0 is the background offset and $w = \frac{1}{2}W\sqrt{ln(4)}$. Red curves reported in figure 4.12 are the best fitted curve from which L has been evaluated to be:

- $\#SFG19010$: L=28.5±0.1nm for G-Ni foam and L=28.9±0.1nm for G-PDMS foam
- $\#SFG19005$: L=42.3±0.1nm for G-Ni foam and L=38.6±0.1nm for G-PDMS foam.

The value did not change after the many steps the samples undergone.

4.5 PMMA infiltration

Due to the properties in the first chapter, PMMA finds a place in different applications such as biomedical, optical, sensor, electronics and energy range. In the study of GF/PMDS foam, PMMA acts as a sacrificial layer. Due to its easy processing, the polymer is a useful support for the graphene structure. PMMA possesses good compatibility with graphene; during the infiltration, it does not alter its properties and in this way permits to act as a template for the next step.
After graphene deposition the foam was infiltrated by PMMA. Several methods were used to achieve the completely filling of pores inside the foam such as contact, suspended, immersion, vacuum, and using a filter membrane. During this step, a solution of PMMA with molecular weight 495K, diluted in 4 % anisole ((**950 PMMA A7**) was used At the end of the process, the samples were cutted in liquid nitrogen in order to characterize them by SEM.
Several problems were encountered during the PMMA infiltration process, for instance:

- Due to the surface tension and viscosity PMMA cannot easily to reach the inside of the Ni scaffold, figure 4.13a shows the free space still existing after PMMA infiltration;
- Temperature annealling is needed to evaporate the solvent, However, the process has to be fast so that PMMA does not dry out before solvent evaporates. Otherwise bubbles get trapped inside the polymer matrix (bubble in figure 4.13b).

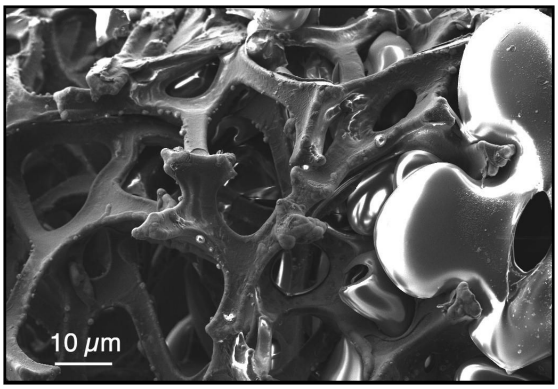

(a)

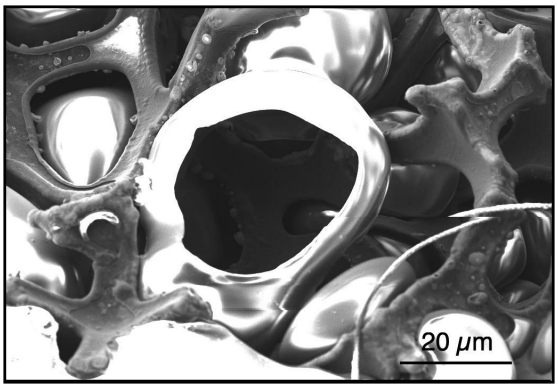

(b)

Figure 4.13: SEM images of Ni-Foam after the infiltration of PMMA

The first method has been applied to sample, the sample $\#SGF19004\_B$ which was placed in **contact** over the hot plate and PMMA was drop casted on the top of it several time. The temperature was raised gradually until 150°C (153,8 ° boiling point of anisole), and the whole process required 3 hours. SEM images collected after the process (figure 4.14a) show the absence of PMMA inside the sample and a superficial crust of PMMA due to a fast dried out which has limited the polymer infiltration.

A second attempt has been applied to samples $\#SGF19004\_D$ and $\#SGF19004\_B$, which were **suspended 2 cm from the hot plate** at 150°C and 120°C, respectively, and PMMA was drop casted on the top of them several times. The suspension enabled PMMA to fill the holes of the foams due to the force of gravity, prevented the accumulation of PMMA in contact with the hot plate which leads to the polymer crust. SEM images collected on samples $\#SGF19004\_D$ (figure 4.14b) and $\#SGF19004\_B$ (figure 4.14c) reveal the successful PMMA infiltration when the hot plat in set at 120°C. However, the process required two days.

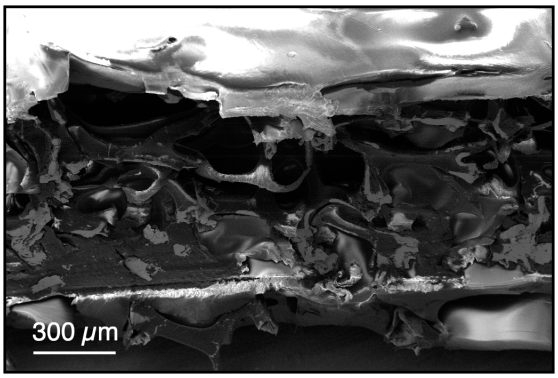

(a) $\#SGF19004\_B$ sample after PMMA infiltration by contact method

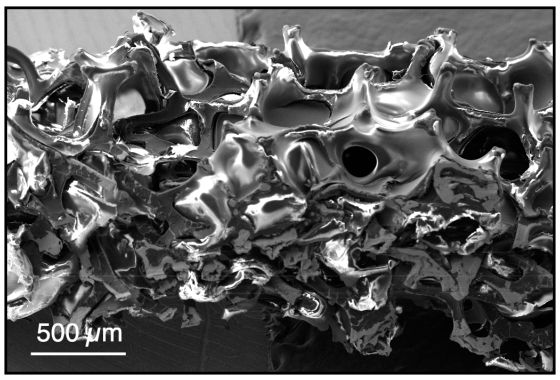

(b) $\#SGF19004_D$ sample after PMMA infiltration by suspension at 150°C

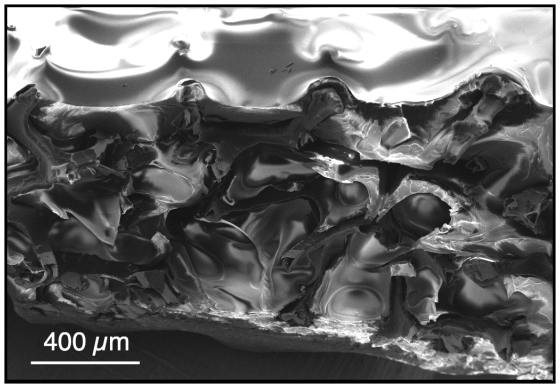

(c) $\#SGF19004_B$ sample after PMMA infiltration by suspension at 120°C

Figure 4.14: SEM images of Ni-Foam after the infiltration of PMMA performed by using differet methods

In order to reduce the duration of the process, the PMMA infiltration were performed in a **vacuum chamber** at 1.6 mbar, after that, samples were placed over the hot plate. Different parameters (vacuum time, temperature of the post thermal treatment) were used:

- Sample #$SGF19001\_A$: 15 minutes in vacuum and 50 minutes over the hot plate at 150 °C;
- Sample #$SGF19001\_B$: 30 minutes in vacuum and 30 minutes over the hot plate at 150 °C;
- Sample #$SGF19001\_C$: 30 minutes in vacuum for each side over the hot plate at 150 °C;

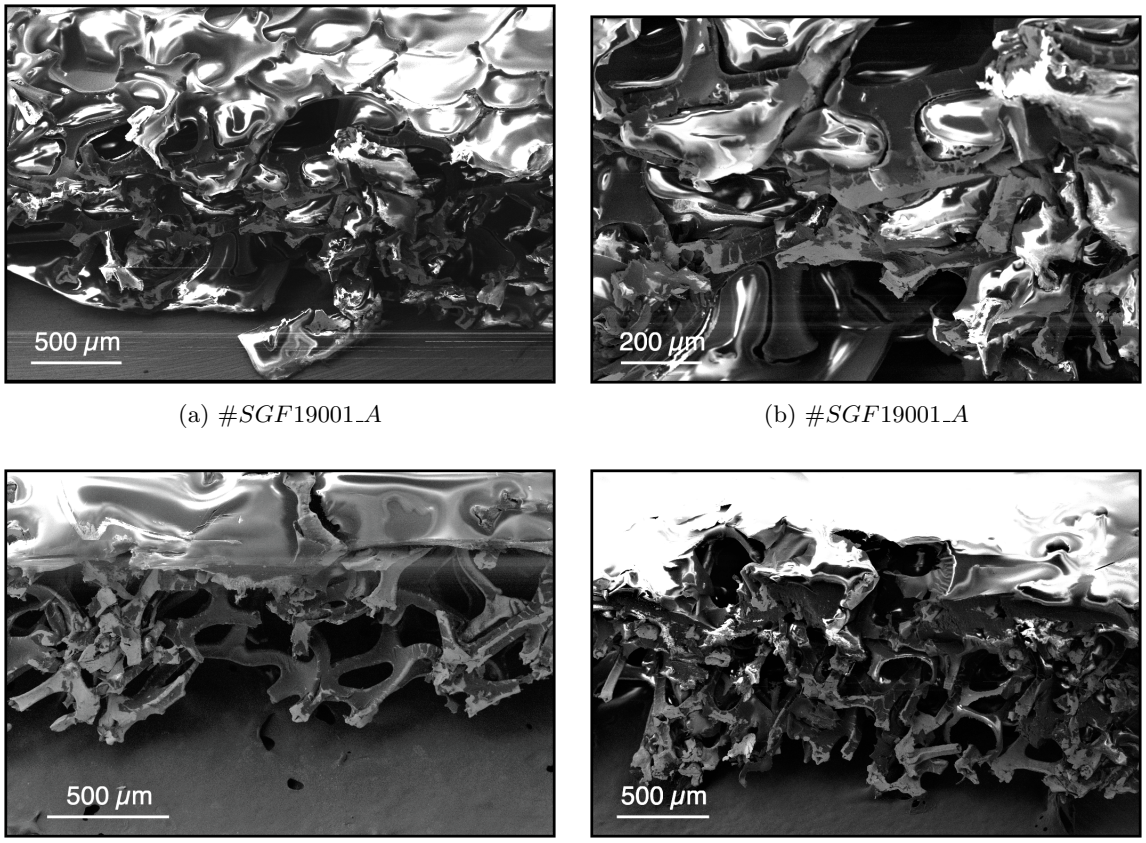

(a) #$SGF19001\_A$ (b) #$SGF19001\_A$

(c) #$SGF19001\_B$ (d) #$SGF19001\_C$

Figure 4.15: SEM images of G-Ni-Foam after the infiltration of PMMA performed in a vacuum chamber at different conditions.

From the SEM images reported in figures 4.15 is possible to notice that PMMA infiltration is achieved at low time in vacuum chamber. This can be explained by the decreasing of the solvent boiling point when pressure is reduced leading the PMMA to explode out of the foam.

PMMA infiltration was then performed by means of a **membrane filter holder**. On samples $SGF19005\_C$ and $SGF19006\_C$ that correspond to the structure of Ni-foam CNR and Ni-foam Politecnico di Torino, respectively. PMMA was drop casted on the top of the sample laid down a membrane, The solution was pumped across the membrane. From the SEM images reported in figure 4.16 it is possible to notice that the polymer completely covers the foam. The SEM images collected with higher magnification (figures 4.16b and 4.16d)) reveal the bad adhesion of PMMA on graphene.

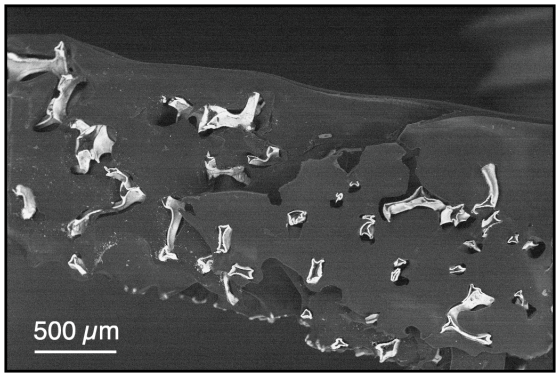

(a) $\#SGF19005\_C$ CNR foam

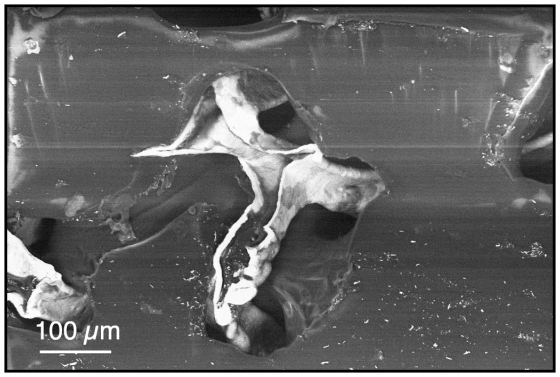

(b) $\#SGF19005\_C$ CNR foam

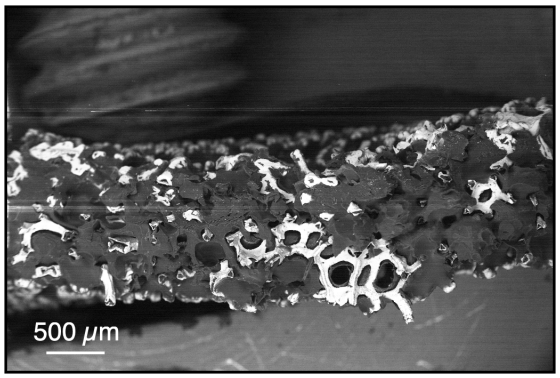

(c) $\#SGF19006\_C$ Politecnico di Torino foam

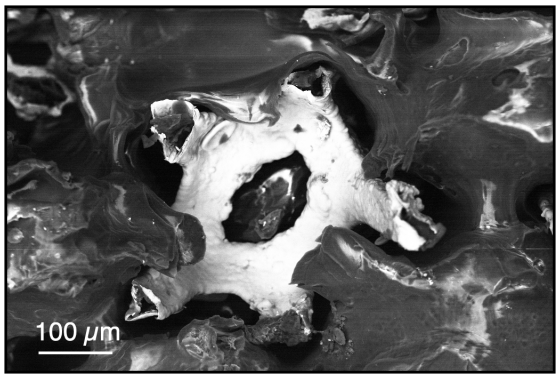

(d) $\#SGF19006\_C$ Politecnico di Torino foam

Figure 4.16: SEM images of G-Ni-Foam after the infiltration of PMMA performed with a membrane filter holder. Figure a) and b) are related to the CNR Ni-foam, instead figure c) and d) correspond to Politecnico di Torino Ni-foam

By summarizing the results obtained from the PMMA infiltration using different methods, it is possible to conclude that:

- PMMA infiltration improves when the annealing temperature is much lower than the boiling point of the solvent (i.e. 153.8°C) which slows down the evaporation of the solvent;
- suspended method permits to infiltrate the foam by exploiting the gravity force; in this way, the polymer is forced to cross the entire sponge, without accumulating on one side of the sample and crust. This technique is improved by the membrane filter holder which guarantees that the foam is filled with PMMA;
- also vacuum method is a proper technique, but for a short time (15 minutes);
- a bad adhesion between PMMA and graphene/Ni matrix has been observed. As a consequence, the free interstices will be filled later by the PDMS. This fact can lead to decrease the conductivity and the the resistivity of device increases.

4.6 Etching of Nickel skeleton

The rigid mechanical properties of Nickel do not allow to achieve flexibility and stretchability that are the main request to the final sensor. Thus, Ni skeleton was etched overnight in $4.5\% FeCl_3$ at $80°C$. After one day, the solution turned green, so it has been changed in a new one. Then, the residual trace of $FeCl_3$ was gently washed in deionized water and removing using $10\% HCl$ at $80°C$ for 8 hours. The etching reaction can be represented by the following chemical reaction [36]:

$$2\,\mathrm{Fe}^{3+}{}_{(\mathrm{l})} + \mathrm{Ni}_{(\mathrm{s})} \longrightarrow 2\,\mathrm{Fe}^{2+}{}_{(\mathrm{l})} + \mathrm{Ni}^{2+}{}_{(\mathrm{l})}$$

As it is possible to see from SEM characterization, (figure 4.17), Ni skeleton is removed.

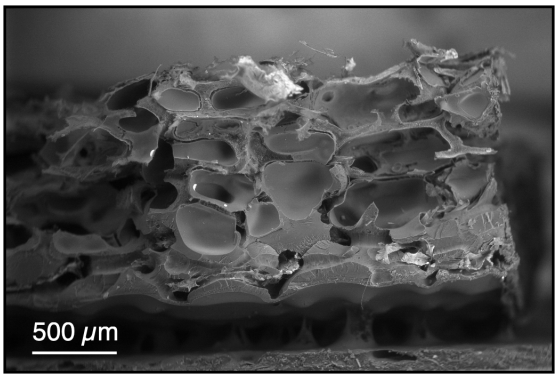

(a) Multilayer graphene layers skeleton incapsulated in PMMA matrix

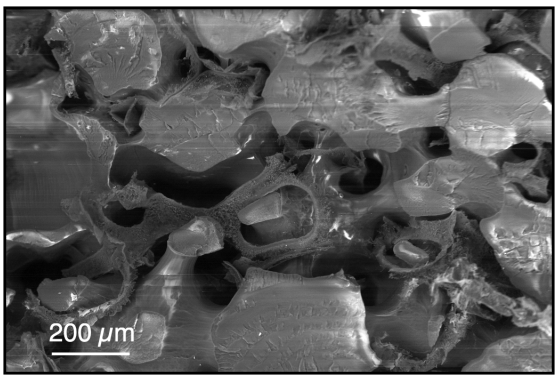

(b) Detail of holes generated by Ni etching

Figure 4.17: SEM images of the sample after Ni removal

The compositional analysis with energy-dispersive X-ray spectroscopy (EDS) of the sample $\#SGF19005$ is reported in figure 4.18. Two different regions are considered: the red rectangle indicates the PMMA, while the blu one is graphene layers. The spectra demostrate that the Ni is totally etched in the red zone (as shown by XRD), but some trace of Fe and Cl are still present.

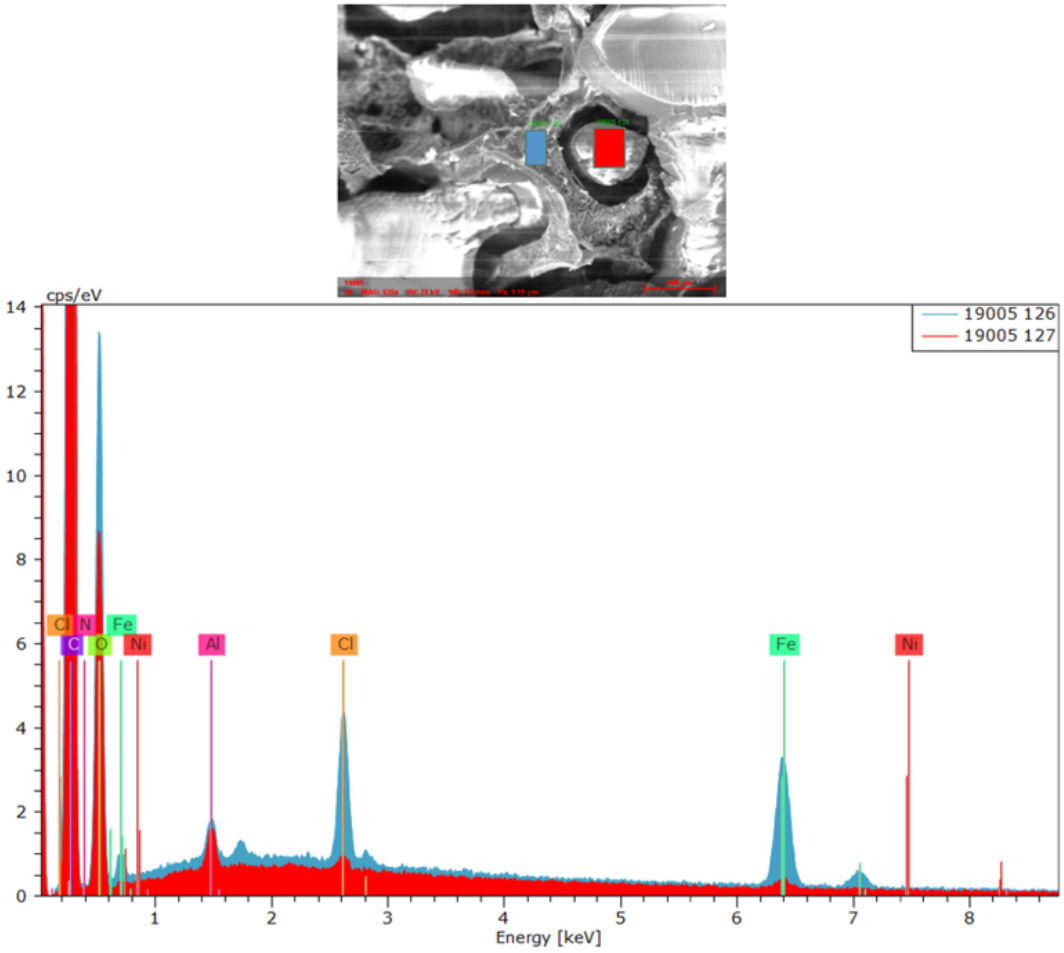

Figure 4.18: EDS analysis of sample $\#SGF19005$

4.7 PDMS infiltration

The following step is the infiltration of the PDMS polymer, in order to guarantee stretchability and resistance of device. In this case the **DOW Corning SYLGARD kit 184** was used, supplied as two-part liquid component kits: the base and the curing agent. In figure 4.19 is reported the apparatus needed to perform the infiltration of the polymer.

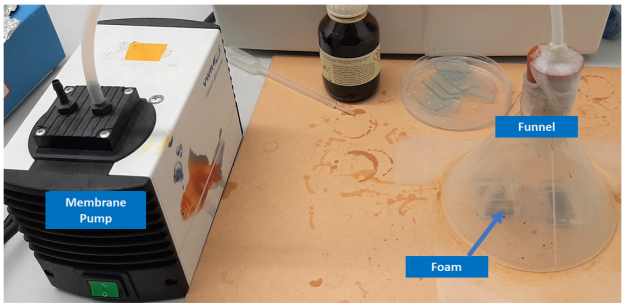

Figure 4.19: PDMS infiltration apparatus

The main steps required to the PDMS infiltration were:

- the base and the curing agent were mixed in a fixed ratio of 5:1;
- the PMMA-Graphene foam was immersed into the polymer. The solution submerged all the sample to ensure pores filling with PDMS;
- to remove air bubbles in the solution, the sample was put over a funnel linked with a membrane pump for 30 minutes.
- The sample was then cured in a furnace at 60 $°C$ for 30 minutes. During this step, the cross-linking of PDMS structure is formed by hydrosilylation reaction [37].

In figure 4.20 is reported the SEM analysis of the section of sample in which the PDMS infiltration was performed. It is possible to distinguish graphene, PDMS and PMMA parts clearly. The white spots are liquid nitrogen trace that was used to cut the foam in order to perform the characterization.

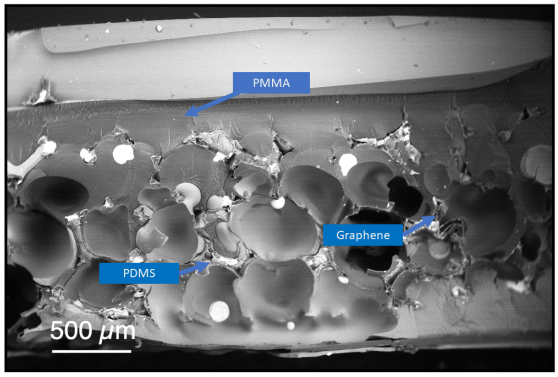

Figure 4.20: SEM image of PMMA-Graphene-PDMS section

The final step consists in removing the PMMA matrix. In order to do that, samples were immersed into acetone solution for two days. The SEM image (figure 4.21) of the PDMS skeleton and graphene confirm that all the steps process are completed. The SEM image collected with higher magnification, (figure 4.22) shows that graphene layers not collapsed and PDMS was correctly infiltrated.

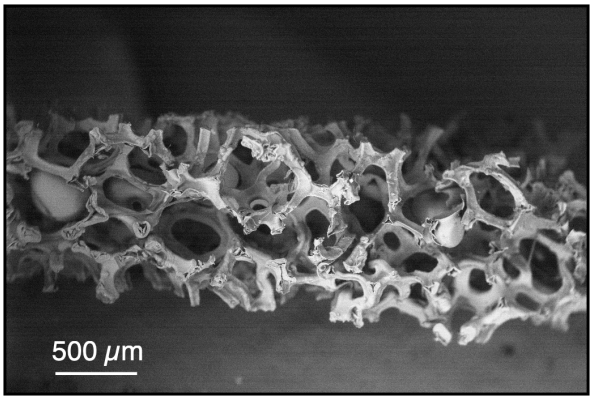

Figure 4.21: SEM image of PDMS-Graphene section

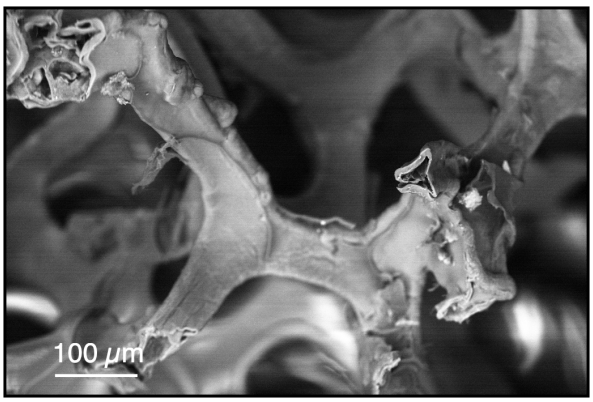

Figure 4.22: SEM image of Graphene-PDMS section

5. Electrical measurements

Flexible sensors due to the high potential, find application in wearable electronics and intelligent systems. The main requests of these sensors are high conductivity, mechanical deformability, materials with a low processing cost, high sensitivity, good flexibility, desired stretchability, biocompatibility and the excellent stability. A flexible sensor is constituted by electrodes, active components and flexible substrate/matrix. In particular, the choice of the polymer substrate is an essential key because it gives necessary properties for stretchability. Graphene, the active material, belongs to the class of materials for high-performance electronics, however, it is not itself stretchable. The graphene/PDMS electrode showed high stretchability both in longitudinal and transverse directions [1]. Besides, due to the excellent properties of graphene, various field can be exploited: pressure sensors, environmental sensors, and stress sensors.[3].
In this chapter, it is analyzed the behaviour of the electrical properties of GF/PDMS when the material is subjected to bending stress, and to compressive stress. Moreover, the effect of the temperature is investigated to establish if the whole system possesses environmental stability. In this sense, the variation of the electrical resistance is studied as a function of different radii of curvature, different forces applied in time, and finally, different temperature.
Figure 5.1 shows the samples tested to measure the variation of electrical resistance.

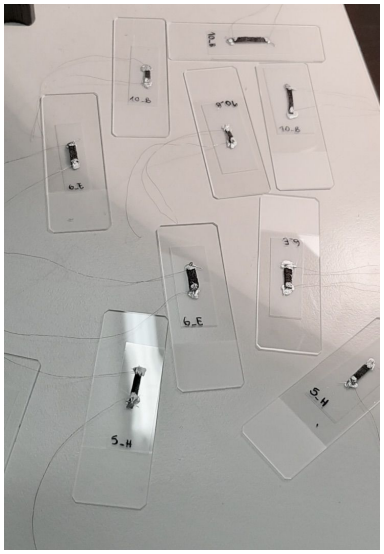

Figure 5.1: Some of GF/PDMS samples having copper wire electrodes contacted with the silver paste

The electrical characterization were performed on samples deriving from two types of depositions:

	FOAM	DEPOSITION
#SGF19005	CNR	38.6±0.1nm
#SGF19010	Politecnico di Torino	28.9±0.1nm

Figure 5.2 shows the GF/PDMS after the removal of PMMA. Then, the sample was cutted into 2 x 0,5 cm^2 and the two extremities were glued to copper wires using a silver paste. All the measurements were performed with an inline two-point probe configuration using a Keithley 2635A source measure unit. In order to avoid the deterioration of the contact during the measure, all the samples were covered with a Kapton adhesive tape.

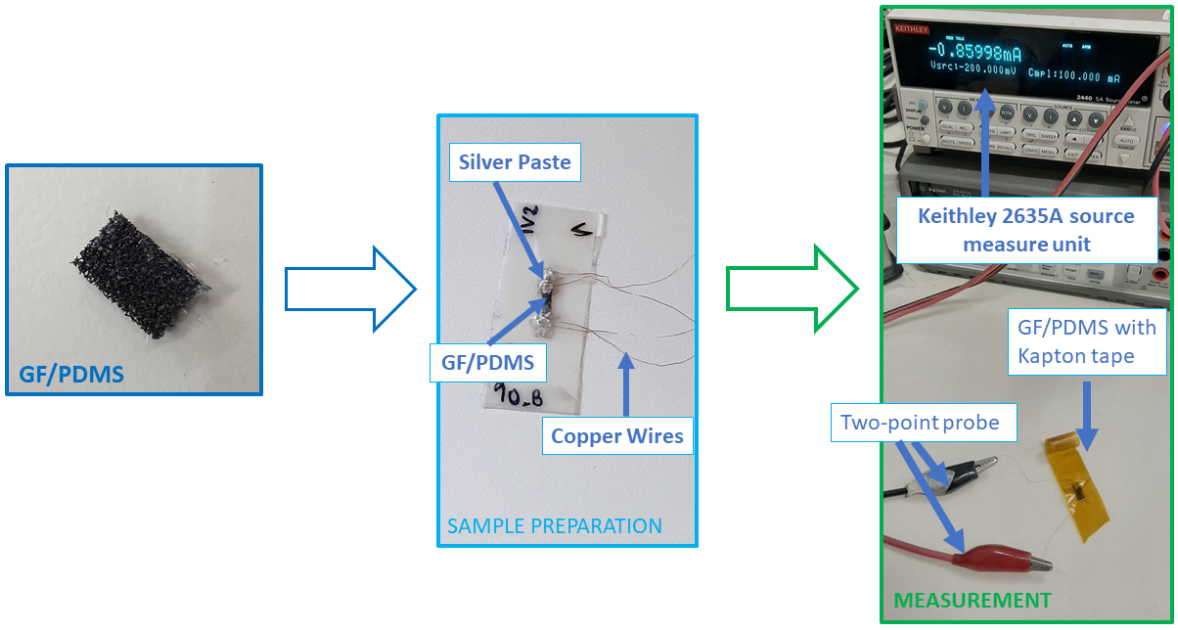

Figure 5.2: GF/PDMS sample after the removal of PMMA, sample preparation and successively resistance measured with Keithley 2635A source measure unit.

The current-voltage (I-V) characteristics were measured in this two terminal configuration with the LabVIEW software (figure 5.3).
From the curve it is possible to calculate the flat resistance of the two samples analyzed:

Sample	Deposition	Electrical Resistance [Ω]
#SGF19005	38.6±0.1nm	48.79
#SGF19010	28.9±0.1nm	341.1

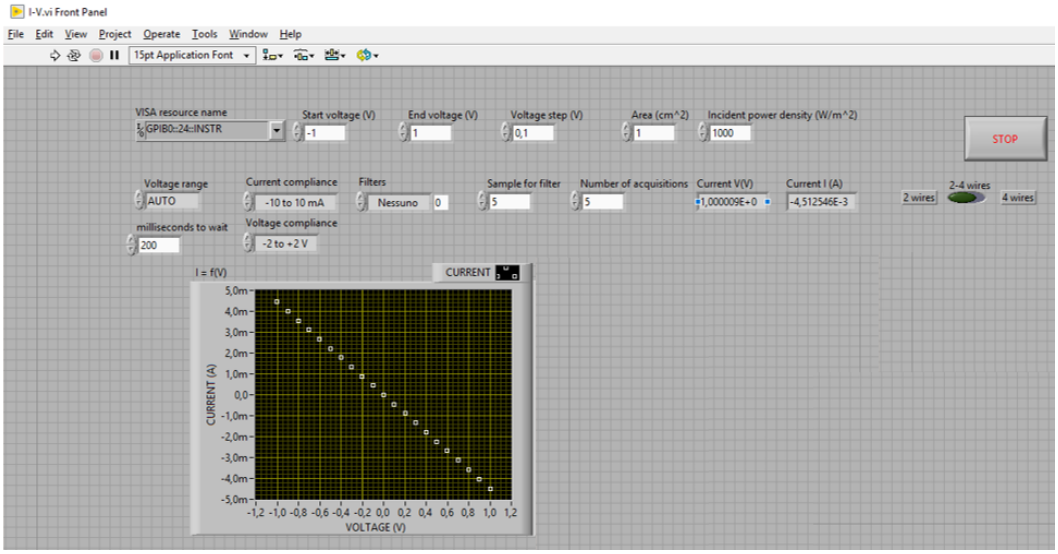

Figure 5.3: LabVIEW software used to obtained the I-V curve

5.1 Bending

The effect of the bending stress on the electrical properties of GF/PDMS was studied. The samples $\#SGF19005$ and $\#SGF19010$ were bended over cylinders with different diameters 3, 4, 5, 6, 8, 9 cm (see figure 5.4).

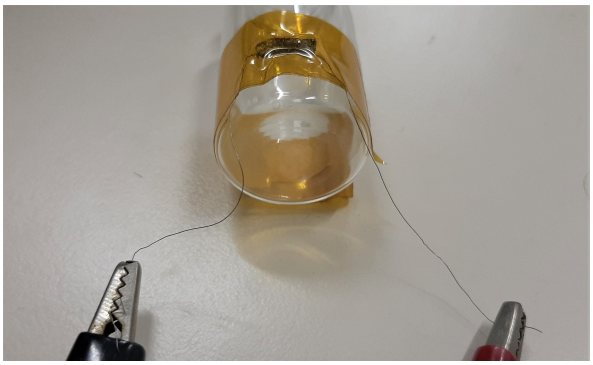

Figure 5.4: Bending of GF/PDMS

From the principle of mechanics, when a material is subjected to bending it is formed a zero stress line also called *neutral axis*. Here, it is possible to have two strains (figure 5.5), depending on the position of the point analyzed. Above the neutral axis, the graphene layers are subjected to tensile stress, while below, they are subjected to compressive stress. The position of the neutral axis depends on the properties of the materials. The distribution of the stress inside the material can be defined by:

$$\sigma = E\frac{y}{\rho} \tag{5.1}$$

in which y is the distance between the point analyzed and the neutral axis, σ represent the stress at the point analyzed, ρ is the bending radius and E is Young's modulus. For a layer bent downwards, if the point analyzed is below the neutral axis, y is positive, and the stress applied is a tensile strain. While if the point is placed below the neutral axis, y is negative and so the stress is compressive [3].

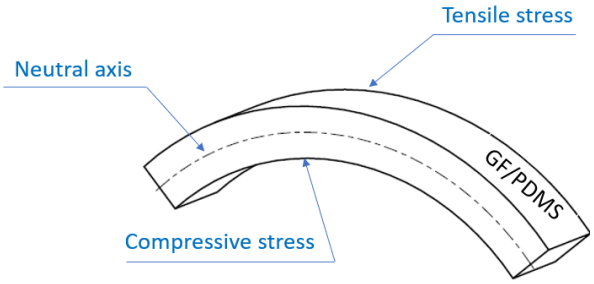

Figure 5.5: Schematic representation of the two strains formed during the bending of GF/PDMS

Figure 5.6 presents the plot of the relative variation of electrical resistance as a function of different bend radius considered. The relative variation of resistance is defined as:

$$\frac{\Delta R}{R_0}[\%] = \frac{R - R_0}{R_0} \tag{5.2}$$

where R_0 is the resistance of the flat sample.
The graph shows that the whole system (GF/PDMS and contact) doesn not respond in a proportional way to the bending stress. Sample $\#SGF19005$ keeps its properties unchanged for the all bend radii tested. Instead, in sample $\#SGF19010$, the variation resistance is unaffected to bending up to $\sim 0,14cm^{-1}$, after that the resistance decreases.

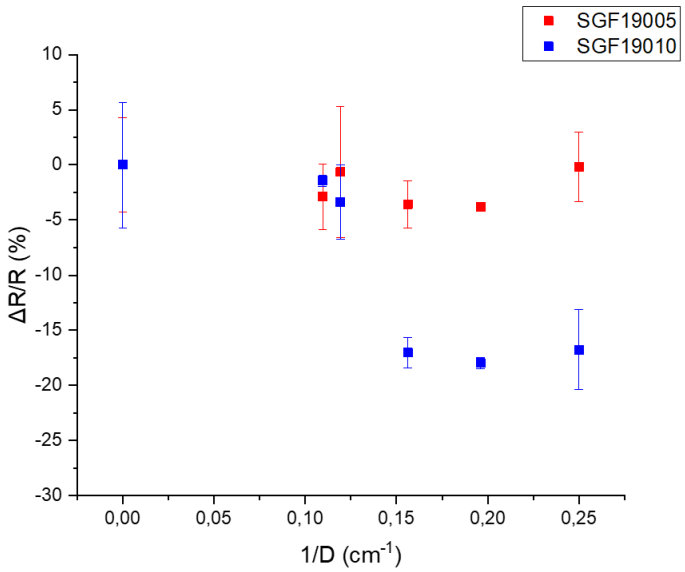

Figure 5.6: Resistance variation vs. 1/D for samples $\#SGF19005$ and $\#SGF19010$

The relative variation of resistance of the two samples can be explained by considering the principles of mechanics analyzed before. When the GF/PDMS is bending, the tensile area is formed above the neutral axis; while below the material is subjected to a compressive strain. The effect of tensile and compressive stress on the electrical properties of the whole system is the opposite resulting in a lower relative variation of resistance [3].

	#SGF19005		#SGF19010	
$1/D$ $[cm^{-1}]$	**R** [Ω]	$\Delta R/R$ [%]	**R** [Ω]	$\Delta R/R$ [%]
0	48,79	0	341,10	0
0,11	47,38	-2,89	336,21	-1,43
0,12	48,48	-0,64	329,61	-3,36
0,16	47,05	-3,56	283,02	-17,08
0,20	46,94	-3,80	279,81	-17,97
0,25	48,71	-0,18	238,92	-16,76

In conclusion, it was found that the system measured (GF/PDMS and the contact with the silver paste) seems to be not suitable to be used as a bending sensor. It is worth noting that in the present study it has not been possible to separate the effects of the mechanical deformations on the GF/PDMS and on the contacts. This is mandatory to fully understand the properties of the system and its possible final applications. For that reason, further studies are planned to develop new strategies for the electrical contacts of the GF/PDMS systems and to separate the above mentioned effects.

5.2 Compression test

GF/PDMS systems have been directly tested to investigate their performances as strain sensors. A mechanical setup was designed to achieve regular compressive stresses on the samples. The setup was composed by a Tirasystem (TV51110) constituted by a shaker (model S51110) powered by an amplifier (model BAA 120) and directly controlled by Vibration Research control unit (VR 9500), and it is associated to software tools. The shaker was placed under a stiff horizontal beam linked to a rigid frame, whose height could be manually controlled by a handwheel. An accelerometer (PCB Piezotronics, model 352C33) was screwed on the vibrating plate of the shaker to give feedback to the controller and to monitor the stress conditions on the samples. A schematic image of the setup system is shown in figure 5.7.

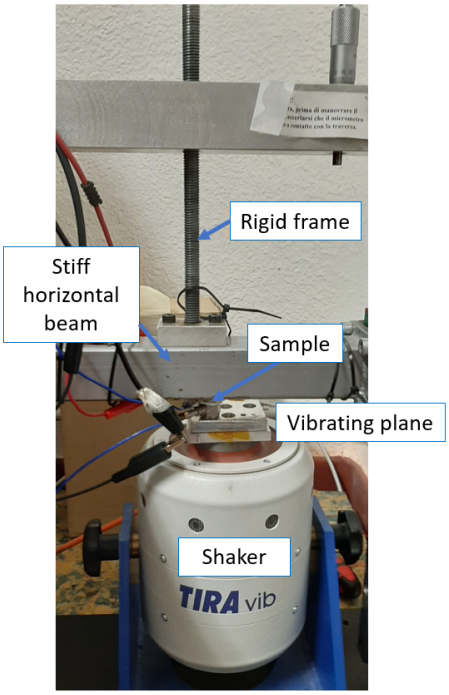

Figure 5.7: experimental set-up used for compression test

Porous foam possesses a common mechanical behaviour under compressive load. Indeed, their stress-strain curve is composed of three main regions: an elastic part for a low stress, a long collapse plateau and then is present a densification zone where the stress rises steeply. The GF monoliths behave, instead, as typical elastic-brittle foam in compression with linear elasticity regions, plateau and then densification regimes. The first region is the response of the individual arms and the GF arm's walls to the strain before any damage. The plateau region is due to the progressive failure of the structure. As more the cell become crushed under compression, opposite arm and GF arm's walls touch themself, and the densification region is formed. Moreover, densification region occurs rapidly for high value of stress (figure 5.8).
Reference [38] demonstrated that when a compression strain is applied to a GF, it responds with a modification of its electrical resistance. A PDMS backbone covered with graphene does not alter the excellent electrical properties of GF, rather it gives mechanical robustness, strength, flexibility and stretchability to the GF. The strain level of GF/PDMS composites depends on the properties of both PDMS and GF.

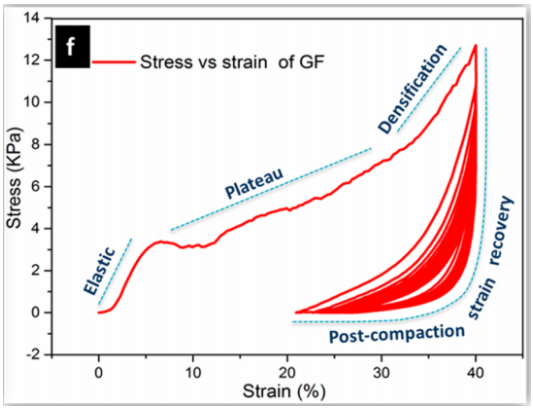

Figure 5.8: Stress-strain curve of GF sample [38]

The electromechanical properties of GF/PDMS has been investigated by measuring its electrical resistance while deforming the composite under cyclic compressive loading with an increasing of the force applied (0.5 N, 3N and 9N).

Figure 5.9 shows the behaviour of sample $\#SGF19005$ as a function of time, for a total time of 300 seconds. In particular, for 0,5 N a variation resistance of $\sim 50\%$ is measured, and for a 3N force applied $\Delta R/R$ is equal to $\sim 100\%$. Lastly, at 9 N the variation of resistance assumes values in a range of $\sim -50\%$ and $\sim 50\%$. For each force applied, the details of the system response for a time frame of 1 second are shown (figures below in figure 5.9). The frequency of the compression loading is 5 Hertz (5 compressions in 1 second). Each compression stimuli is reported (dotted line) superimposed to the response of the system (continuous line). The left y-axis shows the force intensity, while the right y-axis reports the $\Delta R/R$ response of the GF/PDMS composite.

In figure 5.10 is reported the variation of resistance for sample $\#SGF19010$. For 0,5 N the $\Delta R/R$ measured is less than $\sim 10\%$ while for 3N is $\sim 25\%$ with a maximum value of $\sim 40\%$ in 50 seconds. At 9 N, as the previous sample, the variation of resistance assumes values from positive to negative, in this case between $\sim -20\%$ and $\sim 40\%$. By comparing the two figures, it is possible to notice that in the sample $\#SGF19010$ the system deteriorates over time, assuming a less homogeneous trend as the applied force increases. It is worth noticing that the oscillations shown for the 9 N force applied, likely indicate that the GF/PDMS composite is not able to recover the flat/steady state once subjected to a stimuli above a certain value, therefore indicating that the prepared systems have a sort of time-characteristics describing their capability to respond to mechanical loads. These characteristics will be studied in detail in the prosecution of the presented work.

The minimal variation of the resistance is then measured by considering different forces applied (0,1 N, 0,2 N, 0,3 N and 0,5N) in figure 5.11 and figure 5.12. In the table below is reported the $\Delta R/R$ variation obtained for the two samples tested.

	$\#SGF19005$	$\#SGF19010$
Force [N]	$\Delta R/R$ [%]	$\Delta R/R$ [%]
0,1	$\sim -3\%$	$\sim -5\%$
0,2	$\sim 3\%$	$\sim -4\%$
0,3	$\sim 8\%$	$\sim 18\%$
0,5	$\sim 18\%$	$\sim 16\%$

It has to be noticed that the value of $\Delta R/R$ of 0.5 N force is different if compared to the one shown in figure 5.9 and figure 5.10. The reason of this difference relies on the impossibility to measure the same samples, and samples coming from different graphene depositions have been measured. The general behaviour is confirmed, but it comes out clearly that further work is needed to ensure a complete reproducibility of the system response.
Analyzing the data, it is possible to conclude that sample $\#SGF19005$ is highly sensitive to applied compressive strain. On the contrary, the response of sample $\#SGF19010$ is not continuous in time, and the variation of resistance is lower. Literature cannot provide any information about the GF/PDMS with the silver paste when they are subjected to a compressive test. Future works will investigate the relation that link the number of graphene layers deposited to the response to the stress applied.

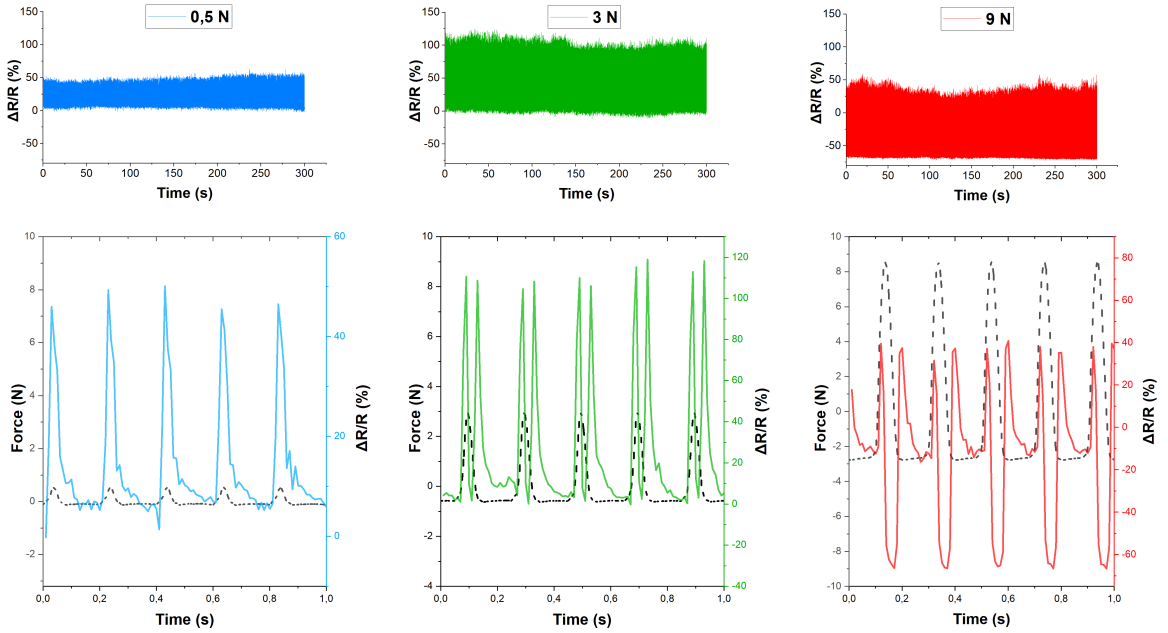

Figure 5.9: Resistance variation as a function of time for sample $\#SGF19005$

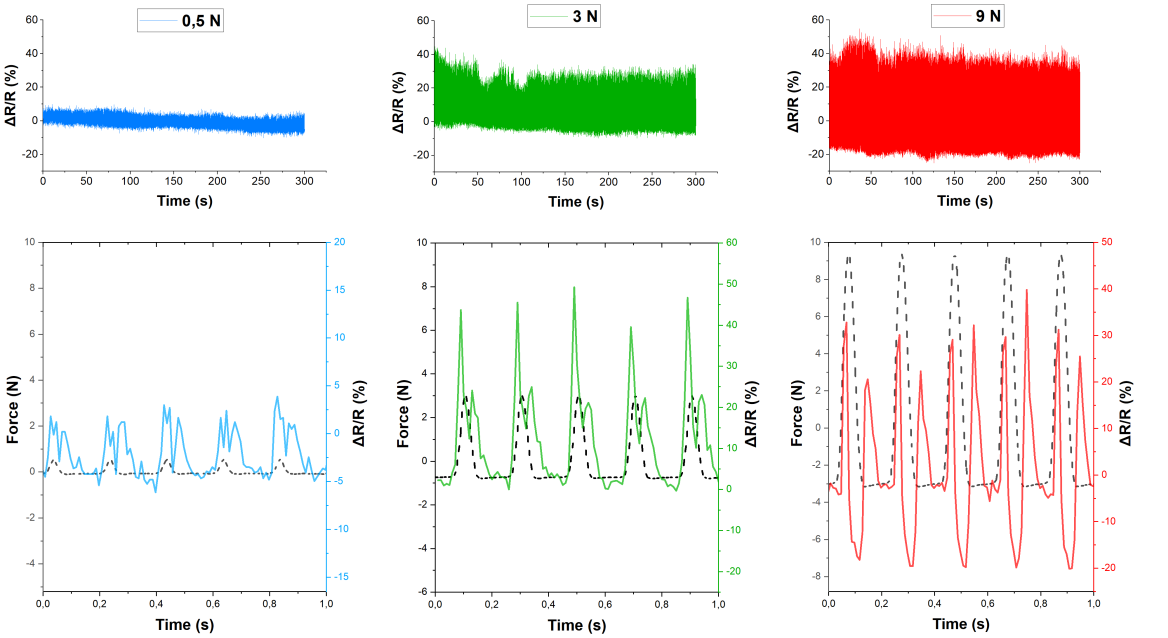

Figure 5.10: Resistance variation as a function of time for sample $\#SGF19010$

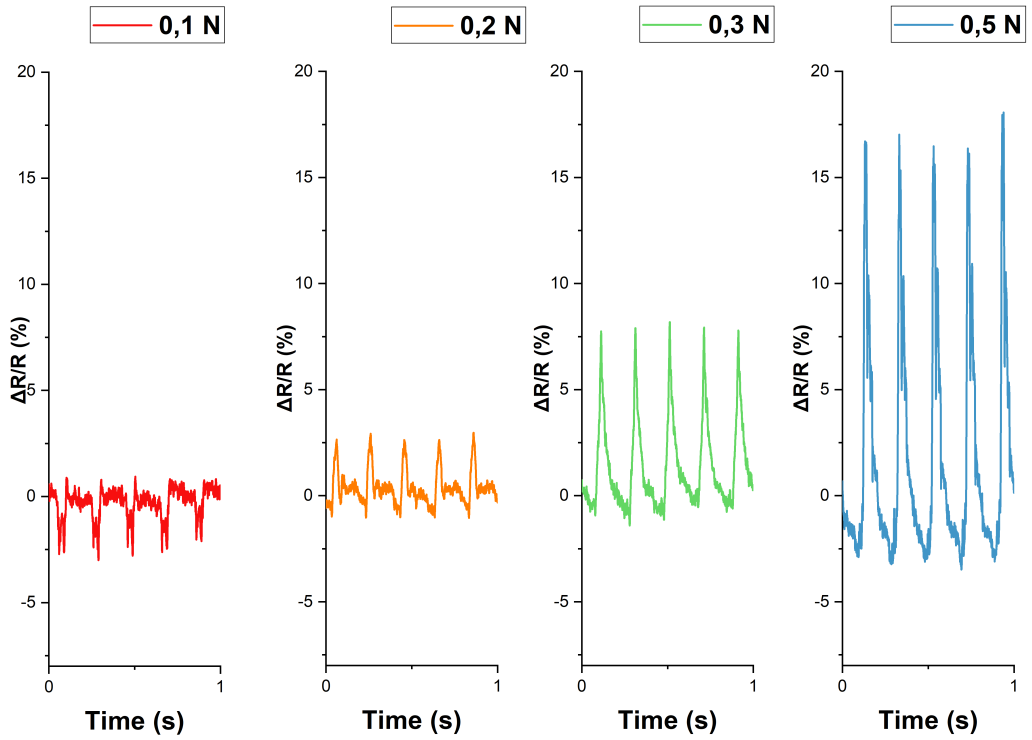

Figure 5.11: Resistance variation during the time for sample $\#SGF19005$ at different force applied.

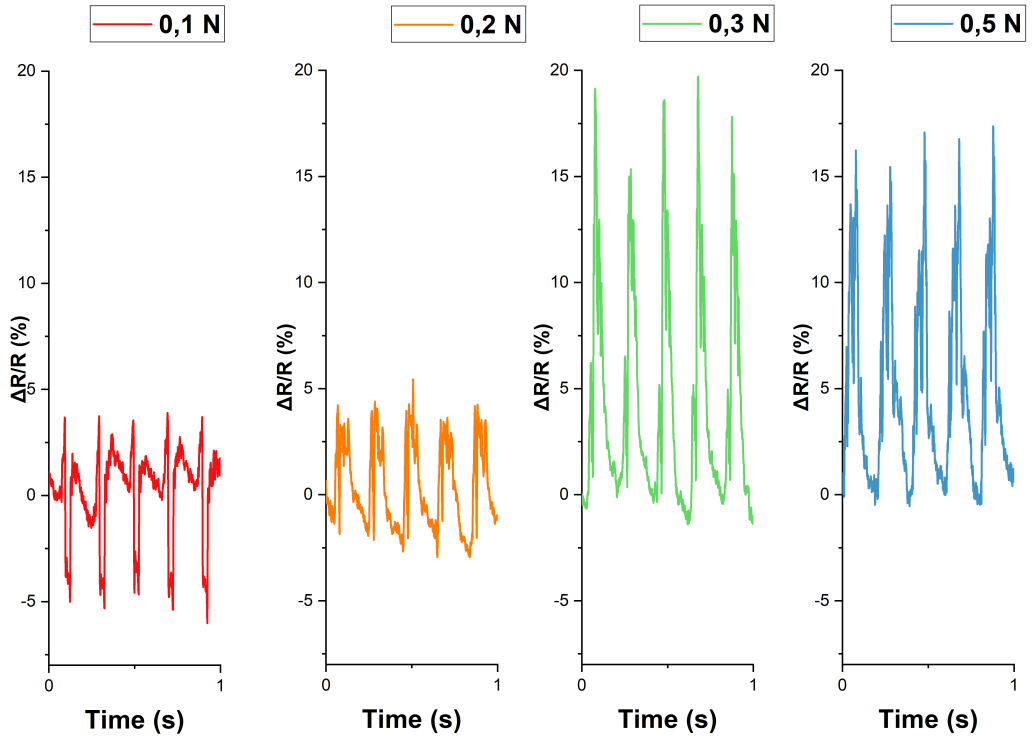

Figure 5.12: Resistance variation during the time for sample $\#SGF19010$ at different force applied.

The trend of the relative resistance variation is then summarized in figure 5.13 which shows that sample $\#SGF19005$ maintains a linear behaviour for different forces applied. On the contrary, for sample $\#SGF19010$, the resistance variation saturates after 0.3 N.

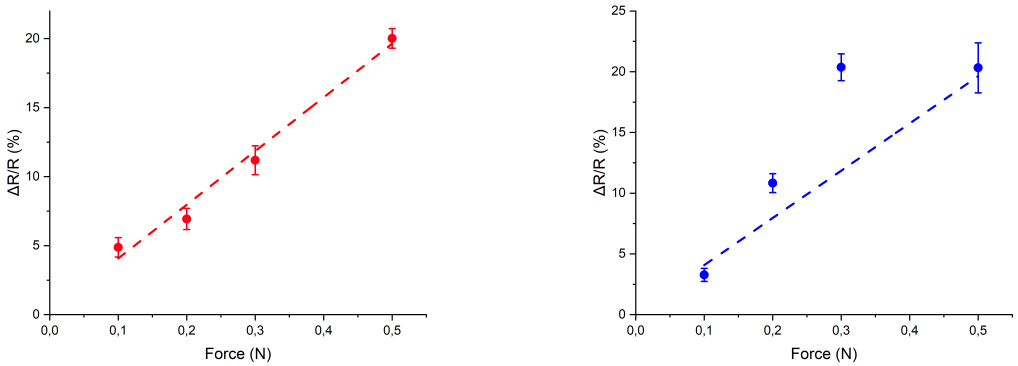

(a) Sample $\#SGF19005$ (b) Sample $\#SGF19010$

Figure 5.13: Resistance variation vs. minimum force applied

After the compression test, the morphology of different GF/PDMS structures obtained with different deposition process parameters was studied with a Zeiss Supra 40 Field Emission SEM (FESEM) equipped with an EDS Oxford Si(Li) spectrometer.
By comparing the FESEM images analysis of the samples $\#SGF19005$ and $\#SGF19010$, it is possible to notice that graphene layers were damage after the compression test. Indeed, from the image it is clearly distinguish the PDMS skeleton and the graphene broken layers indicate with a blue arrow. After the compression test, the graphene deposited on the sample $\#SGF19005$ is more damaged than the sample $\#SGF19010$. The damaging observed on sample $\#SGF19005$ is in line with the XRD results: the graphene multilayer thickness evaluated from XRD measurements after the electrical characterization is 38 nm, lower than the one obtained after CVD process (42nm).

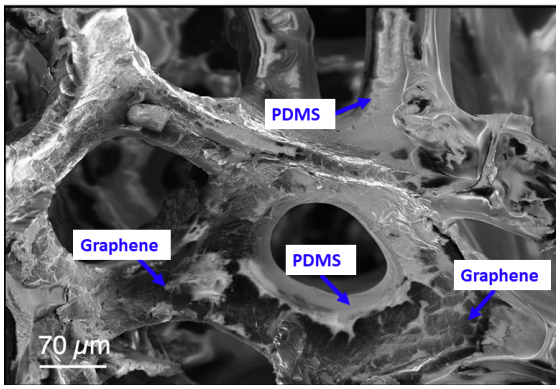

(a) Sample #$SGF19005$

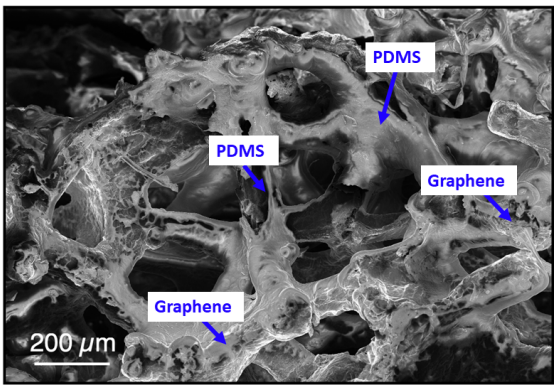

(b) Sample #$SGF19010$

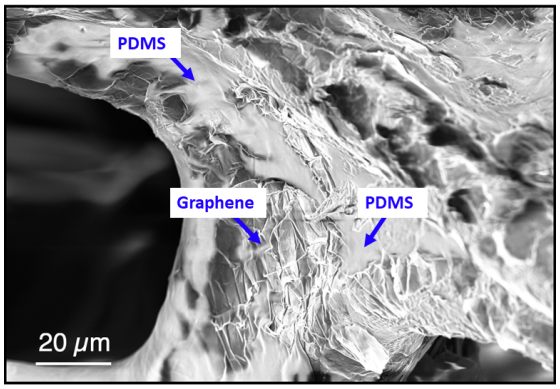

(c) Sample #$SGF19005$

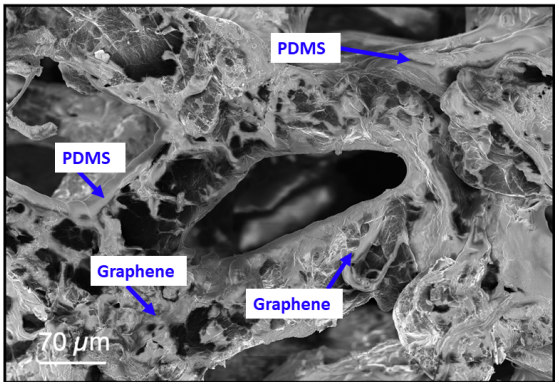

(d) Sample #$SGF19010$

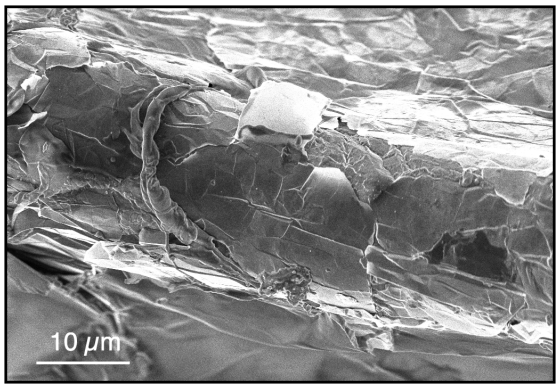

(e) Sample #$SGF19005$

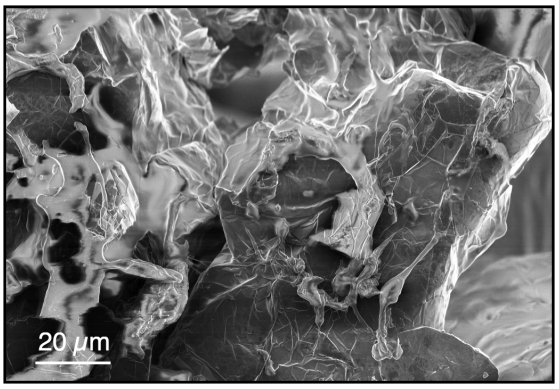

(f) Sample #$SGF19010$

Figure 5.14: Morphology characterization of the sample after the compression test

5.3 Temperature

The variation of the electrical resistance as a function of the temperature was measured in an oven (Memmert 30-1060) equipped with cables feedthroughs to perform the electrical measurements. In figure 5.15 the variation of resistance $\Delta R/R$ is reported as a function of temperature.

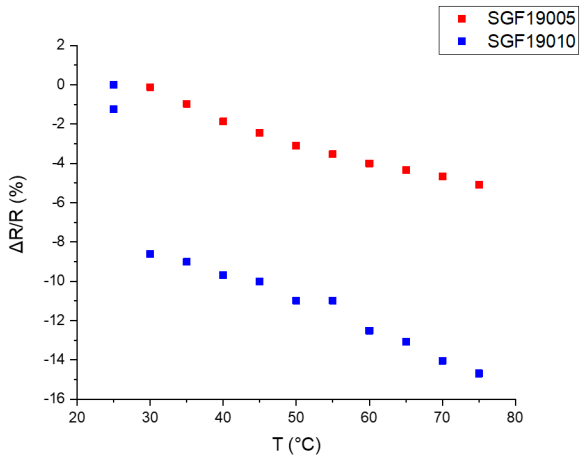

Figure 5.15: Resistance variation as a function of temperature

The variation of the resistance decreases in an almost linear way with the increases of temperature. The values obtained from the measurement are summarize in the table below:

	$\#SGF19005$		$\#SGF19010$	
Temperature $°C$	**R** [\Ω]	$\Delta R/R$ [%]	**R** [\Ω]	$\Delta R/R$ [%]
25	42,21	0	236,77	0
30	42,16	-0,11	238,48	-8,61
35	41,80	-0,97	238,23	-9,01
40	41,42	-1,87	235,42	-9,69
45	41,18	-2,44	232,28	-10,02
50	40,90	-3,10	228,63	-10,98
55	40,72	-3,52	226,37	-10,98
60	40,52	-4,00	222,03	-12,51
65	40,38	-4,33	223,48	-13,08
70	40,24	-4,66	220,13	-14,04
75	40,06	-5,09	221,21	-14,69
After measurement ($@T = 25°C$)	42,21	0	241,96	-1,24

The measurements after $75°C$ have been performed waiting for the system to cool down naturally to room temperature ($25°C$).

Figure 5.15 is in accordance with the reference [3] where the result is shows in figure 5.16.

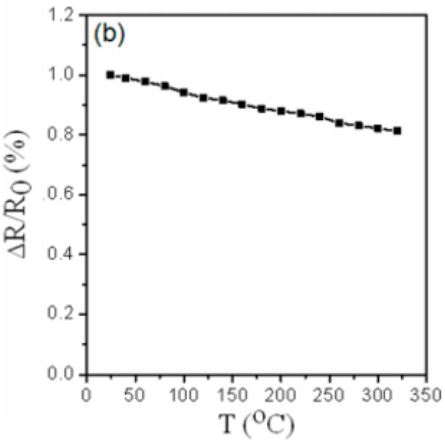

Figure 5.16: Figure from reference [3] where the variation of the resistance is plotted as a function of the temperature

The negative trend measured can be explained by considering the temperature coefficient of resistance (TCR). Indeed, it is a key parameter to evaluate the temperature sensing properties of a material. It is defined as the relative change of resistance per degree of temperature change:

$$TCR = \frac{R_2 - R_1}{R_1}(T_2 - T_1) \tag{5.3}$$

where T_1 and T_2 are the initial and final temperature respectively that correspond to the value R_1 and R_2 [39]. Moreover, high TCR value provides high sensitivity for resistance-type temperature sensors. TCR value is dynamically changed at different temperature ranges for certain materials. For the metal TCR is positive, means that the resistance increase with the increasing of the temperature. For other materials, such as carbon, silicon and germanium, TCR is negative, and so a decrease of resistance occurs for an increase of temperature [40].
For sample $\#SGF19005$ and $\#SGF19010$, it is possible to calculate the TCR considering the value of resistance at $25°C$ and $75°C$.

- sample $\#SGF19005$: TCR = -2,54 $[1/°C]$
- sample $\#SGF19010$: TCR = -3,28 $[1/°C]$

In conclusion, it was found that the analyzed systems (GF/PDMS and the contacts with the silver paste) show a negative TCR, that is in qualitatively in agreement with the data reported in literature for graphene films. Based on the reported data, it must be taken into account that the GF/PDMS systems show a not negligible response to temperature variations. From one side, this indicates that these composites can be used not only as compression sensors, but also as flexible temperature sensors, in a wide range of temperature values. On the other side, if the systems will be used as compression sensors in changing environment conditions, the two effects must be carefully separated. It is worth noticing that a better understanding of the temperature response of these systems is mandatory, both from the experimental and from the modeling point of views. The latter can be carried out by Finite Element Method (FEM), as done, for example, in Ref. [41], where, however, the system is different from ours (a composite made by the GF filled with PDMS), suggesting that it a FEM study of the systems proposed in this work has still to be carried out and can be extremely useful for the whole understanding of their behaviour.

6. Conclusion and future work

The presented study has been focused on the development of an experimental methodology for the fabrication of 3D composites made by CVD grown graphene foams with an internal PDMS backbone, using Ni foams as starting templates, for stretchable sensing applications.

Firstly, two different structures of Ni templates were analyzed, one provided by Politecnico di Torino and the other from CNR-Bologna. Ni template from CNR is characterized, by pores with diameter in the range of 120 to 380 μm and an almost circular section. The Ni-templates from Politecnico di Torino showed pores with diameter ranging between 160 to 450 μm with hollow branches and stretched circular shapes. Two different Chemical Vapor Deposition processes for the synthesis of graphene on the Ni templates have been considered. Sample $\#SGF19005$ indicates a graphene foam grown on the CNR Ni template with a flux of 50 sccm of CH_4 and a deposition time of 10 minutes, resulting in a thicker layer of graphene. Sample $\#SGF19010$ indicates instead a graphene foam grown on the Politecnico di Torino Ni template with a flux of 50 sccm of CH_4 and a deposition time of 5 minutes, resulting in a thinner layer of graphene. After the deposition process, both samples have been subjected to PMMA infiltration. Different methods were tested with the aim to completely fill the hollow structure of the graphene foams. Trough SEM observation it has been demonstrated that the result has been achieved performing the infiltration process in a vacuum chamber for a short time or by means of a membrane filter holder. Following steps in the preparation of the final composites have been the chemical etching of the Ni template followed by its substitution with infiltrated PDMS. last step has been the PMMA removal, to obtain finally a graphene foam with a PDMS backbone.

All samples were characterized using different techniques. SEM analysis was performed to provide information on the morphology and to control each process step, while with EDS the effectiveness of the removal of Ni template was verified.
Raman spectroscopy analysis allowed us to evaluate the quality of graphene deposited. From the Raman spectra of a sample $\#SGF19005$, the characteristic peaks demonstrated a high quality of crystalline multilayer without defects. In sample $\#SGF19006$, reference sample with a thick layer deposited on top, the Raman spectra shows a defective multilayer graphene structure. Also, in sample $\#SGF19010$ the graphene is a multilayer structure. Moreover, Raman spectra showed some traces of PMMA residuals, meaning that it was not completely removed in the acetone solution.
With XRD techniques, the number of the layer deposited was analyzed, both after the CVD process and at the end of GF/PDMS fabrication. From the analysis, the thickness of the graphene multilayer present in $\#SGF19005$ after the deposition was 28,5 nm, while at the end of the process was 28,9 nm. In sample $\#SGF19010$, the thickness of the multilayer was 42,3 nm after the synthesis and at the end of the process was 38,6 nm. This characteristic values did not change after the successive steps.

The electrical measurements of GF/PMDS were performed on the composite subjected to bending stress (by considering different diameters), to compressive stress (at different applied forces). Moreover, the environmental stability of the composite was studied as the electrical resistance variation as

a function of the temperature changes.

From the bending test, it was found that the system composed by GF/PDMS and the silver paste contacts does not respond in a proportional way to the stress applied. Indeed, in sample $\#SGF19005$, the variation of electrical resistance is unchanged for all the diameters tested. In sample $\#SGF19010$, instead, the $\Delta R/R$ is unaffecting by bending up to 0,14 cm^{-1}. In this sense, the GF/PDMS and the contact seems not to be suitable to be used as a bending sensor.

The compressive test demonstrated that the sample with a thick graphene layer, $\#SGF19005$, is more sensitive to the variation of force applied rather than the $\#SGF19010$, which is characterized by a thinner graphene layer. In particular, the variation of electrical resistance for sample $\#SGF19005$ is increased from ∼50 % up to a positive and negative value (from ∼-50 % to ∼50 %) for 9 N force applied. The variation in resistance of sample $\#SGF19010$ was in the range of ∼10 % for 0,5 N force up to a positive and negative value (from ∼-20 % to ∼40 %). The response over time of sample $\#SGF19010$ is not continuous. The minimal variation of the resistance was also measured by considering different force applied. Again, sample $\#SGF19005$ is able to respond to the force applied with a more significant variation of resistance than sample $\#SGF19010$.

Successively, the variation of electrical resistance of the GF/PDMS composites was tested as a function of the temperature. The data obtained show a decrease in the resistance as the temperature is rising up to 75°C. The range of temperature was set from 25°C to 75°C, with the aim of understanding if the sensor is adequate to daily life functioning and if it possesses enough environmental stability. A better understanding of the temperature response of these systems is mandatory, both from the experimental and from the modeling point of views. As said in Chapter 5, GF/PDMS can act as compression sensors but also as flexible temperature sensors in a wide range of temperature values. On the other hand, if the systems is used as compression sensors in changing environment conditions, the two effects must be carefully separated. The temperature respond of the system can be theoretically modeled, to support the experimental results, by Finite Element Method (FEM), a powerful tool to discriminate between the response of the sensor to a temperature variation from a compressive stress applied on the same sensor.

In conclusion, thank to the results achieved in this study, it can be said that the GF/PDMS composites confirm their potentialities as materials for flexible sensing applications. They can be used as compression sensors as well as as flexible temperature sensors, in a wide range of temperature values. It is worth mentioning that the main problem encountered during the electrical measurement has been to separate the contribution coming from the mechanical deformation of the GF/PDMS composites and the one arising from the silver paste contacts, that exhibited a well pronounced instability during the tests. Further studies are planned to fully understand the properties of the system and to separate these two contributions. Moreover, new strategies for the electrical contacts are planned. Future works will include also the investigation of the link between the characteristics of the grown graphene films (number of layers, defectiveness) and the response of the system to mechanical and thermal stimuli.

References

[1] Yonghee Kim et al. "Deformable and Stretchable Electrodes for Soft Electronic Devices". In: *Macromolecular Research* 27.7 (2019), pp. 625–639. DOI: 10.1007/s13233-019-7175-4.

[2] Mengting Chen et al. "Highly Stretchable Conductors Integrated with a Conductive Carbon Nanotube/Graphene Network and 3D Porous Poly(dimethylsiloxane)". In: *Advanced Materials* (2014). DOI: 10.1002/adfm.201401886.

[3] Rongqing Xu et al. "Facile Fabrication of Three-Dimensional Graphene Foam/Poly(dimethylsiloxane) Composites and Their Potential Application as Strain Sensor". In: *Appl. Mater. Interfaces* (2014), pp. 13455–13460.

[4] Zongping Chen et al. "Three-dimensional flexible and conductive interconnected graphene networks grown by chemical vapour deposition". In: *Nature materials* 10 (2011), pp. 424–8. DOI: 10.1038/nmat3001.

[5] Adeyinka Idowu, Benjamin Boesl, and Arvin Agarwal. "3D graphene foam-reinforced polymer composites-A review". In: *Elsevier* (2018). DOI: 10.1016/j.carbon.2018.04.024.

[6] Y. Oshida. *Bioscience and Bioengineering of Titanium Materials*. Second Edition. Oxford: Elsevier, 2013. Chap. 12, pp. 457–497. ISBN: 978-0-444-62625-7. DOI: 10.1016/B978-0-444-62625-7.00012-1.

[7] P.S. Liu and G.F. Chen. *Application of Porous Metals*. Butterworth-Heinemann, 2014. Chap. 3, pp. 113–188. ISBN: 978-0-12-407788-1. DOI: 10.1016/B978-0-12-407788-1.00003-4.

[8] M.F. Ashby et al. *Characterization methods*. Butterworth-Heinemann, 2000. Chap. 3, pp. 24–39. ISBN: 978-0-7506-7219-1. DOI: 10.1016/B978-075067219-1/50005-2.

[9] Yanwu Zhu et al. "Graphene and graphene oxide: Syntesis, Properties and Applications". In: *Advanced Materials* (2010). DOI: 10.1002/adma.201001068.

[10] H. Cheun Lee et al. "Review of the Synthesis, transfer, characterization and growth mechanisms of single and multilayer graphene". In: *The Royal Society of Chemistry* (2017). DOI: 10.1039/c7ra00392g.

[11] Geim A.K. and Novoselov K.S. "The rise of graphene". In: *Nature Mater* (2007), pp. 183–191. DOI: 10.1038/nmat1849,.

[12] Mohammad Khan, Mohammad Mansoob Khan, and Moo Hwan Cho. "Recent Progress of Metal-Graphene Nanostructures in Photocatalysis". In: *Nanoscale* 10 (2018). DOI: 10.1039/C8NR03500H.

[13] Castro Neto et al. "The electronic properties of graphene". In: *Reviews of Modern Physics* 81.1 (2009), pp. 109–162. ISSN: 1539-0756. DOI: 10.1103/revmodphys.81.109.

[14] G. Kalita and M. Tanemura. "Fundamentals of Chemical Vapor Deposited Graphene and Emerging Applications". In: *Graphene Materials*. Rijeka: IntechOpen, 2017. Chap. 3. DOI: 10.5772/67514.

[15] Dodd Gray, Adam McCaughan, and Bhaskar Mookerji. "Electronic Band Structure of Graphene". In: *6.730–Physics for Solid State Applications* (2009).

[16] F. Utermohlen. *Tight-Binding Model for Graphene*. 2018.

[17] Pere Miró, Martha Audiffred, and Thomas Heine. "An atlas of two-dimensional materials". In: *Chem. Soc. Rev.* 43 (18 2014), pp. 6537–6554. DOI: 10.1039/C4CS00102H.

[18] K. S. Novoselov et al. "Two-dimensional gas of massless Dirac fermions in graphene". In: *Nature* 438 (2005), pp. 197–200.

[19] "Manufacturing Processes for Engineering Materials,Serope Kalpakjian". In: *Journal of Applied Metalworking* 3.4 (1985), pp. 446–446. ISSN: 0162-9700. DOI: 10.1007/BF02833667.

[20] J. L. Halary, F. Laupretre, and L. Monnerie. *Polymer Materials: Macroscopic Properties and Molecular Interpretations*. John Wiley & Sons, 2011. ISBN: 978-0-470-61619-2.

[21] Umar Ali, Khairil Juhanni Bt. Abd Karim, and Nor Aziah Buang. "A Review of the Properties and Applications of Poly (Methyl Methacrylate) (PMMA)". In: *Polymer Reviews* 55.4 (2015), pp. 678–705. DOI: 10.1080/15583724.2015.1031377.

[22] Xueji Zhang et al. "Exposure strategies for polymethyl methacrylate from in situ x-ray absorption near edge structure spectroscopy". In: *Journal of Vacuum Science & Technology B: Microelectronics and Nanometer Structures* 13 (1995), pp. 1477–1483. DOI: 10.1116/1.588175.

[23] S. Vlassov et al. "Adhesion and mechanical properties of PDMS-based materials probed with AFM: a review". In: *Macromolecular Research* 56 (2018), pp. 62–78. DOI: 10.1515/rams-2018-0038.

[24] Pierson and Hugh O. *Handbook of Chemical Vapour Deposition: Principles, Technology and Applications*. Elsevier Science, 1999. Chap. 2,3,5.

[25] Walter Scot Ruska. *Microelectronic processing: an introduction to the manufacture of integrated circuits*. McGraw-Hill Ryerson, 1987. Chap. 8.

[26] Richard C. Jaeger. *Introduction to Microelectronic Fabrication*. Vol. Volume 5 di Modular series on solid state devices. Prentice Hall, 2002. Chap. 6.

[27] Yang Leng. *Materials Characterization: Introduction to Microscopic and Spectroscopic Methods*. Wiley-VCH Verlag GmbH & Co. KGaA, 2013. ISBN: 9783527334636.

[28] "Silicon drift detectors for high resolution room temperature X-ray spectroscopy". In: *Nuclear Instruments and Methods in Physics Research Section A: Accelerators, Spectrometers, Detectors and Associated Equipment* 377.2 (1996), pp. 346–351. ISSN: 0168-9002. DOI: 10.1016/0168-9002(96)00210-0.

[29] Raimund Horn. "Script to Lecture Raman Spectroscopy". In: (2009).

[30] Yi Zhang, Luyao Zhang, and Chongwu Zhou. "Review of Chemical Vapor Deposition of Graphene and Related Applications." In: *Accounts of chemical research* (2013), pp. 2329–2339.

[31] Maria Losurdo et al. "Graphene CVD growth on copper and nickel: role of hydrogen in kinetics and structure". In: *Phys. Chem.* 13 (46 2011), pp. 20836–20843. DOI: 10.1039/C1CP22347J.

[32] Van Luan Nguyen and Young Hee Lee. "Towards Wafer-Scale Monocrystalline Graphene Growth and Characterization". In: *Small* 11.29 (2015), pp. 3512–3528. DOI: 10.1002/smll.201500147.

[33] H. Naseem K. Al-Shurman. "CVD Graphene Growth Mechanism on Nickel Thin Films". In: *Excerpt from the Proceedings of the 2014 COMSOL Conference in Boston* (2014).

[34] L.M. Malard et al. "Raman spectroscopy in graphene". In: *Physics Reports* 473.5 (2009), pp. 51–87. ISSN: 0370-1573. DOI: 10.1016/j.physrep.2009.02.003.

[35] Andrea C. Ferrari. "Raman spectroscopy of graphene and graphite: Disorder, electron–phonon coupling, doping and nonadiabatic effects". In: *Solid State Communications* 143.1 (2007), pp. 47–57. ISSN: 0038-1098. DOI: 10.1016/j.ssc.2007.03.052.

[36] C. Hong-Kyw et al. "Characterization of chemical vapor deposition-grown graphene films with various etchants". In: *Carbon letters* 13 (1 2012). DOI: 10.5714/CL.2012.13.1.044.

[37] A.C.C. Esteves et al. "Influence of cross-linker concentration on the cross-linking of PDMS and the network structures formed". In: *Polymer* 50.16 (2009), pp. 3955–3966. ISSN: 0032-3861. DOI: https://doi.org/10.1016/j.polymer.2009.06.022. URL: http://www.sciencedirect.com/science/article/pii/S0032386109004911.

[38] Yarjan Abdul Samad et al. "Novel Graphene Foam Composite with Adjustable Sensitivity for Sensor Applications". In: *ACS Applied Materials & Interfaces* 7.17 (2015), pp. 9195–9202. DOI: 10.1021/acsami.5b01608.

[39] M. M. Hussain and N. El-Atab. *Handbook of Flexible and Stretchable Electronics*. CRC Press, 2019. ISBN: 9781315112794. DOI: 10.1201/b22262.

[40] Xuewen Wang, Zheng Liu, and Ting Zhang. "Flexible Sensing Electronics for Wearable/Attachable Health Monitoring". In: *Small* 13.25 (), p. 1602790. DOI: 10.1002/smll.201602790.

[41] Ya-Fei Zhang et al. "Numerical simulation of thermal conductivity of graphene filled polymer composites". In: *Composites Part B: Engineering* 106 (2016), pp. 324–331. ISSN: 1359-8368. DOI: j.compositesb.2016.09.052.

[42] Ashby et al. *Metal Foams: A Design Guide*. Elsevier Science, 2000. ISBN: 9780080511467.

[43] Yi Zhang, Luyao Zhang, and Chongwu Zhou. "Review of Chemical Vapor Deposition of Graphene and Related Applications". In: *Accounts of Chemical Research* 46.10 (2013), pp. 2329–2339. DOI: 10.1021/ar300203n.

[44] Abhijit Ganguly et al. "Probing the Thermal Deoxygenation of Graphene Oxide Using High-Resolution In Situ X-ray-Based Spectroscopies". In: *The Journal of Physical Chemistry C* 115.34 (2011), pp. 17009–17019. DOI: 10.1021/jp203741y.

[45] Yarjan Abdul Samad et al. "Graphene Foam Developed with a Novel Two-Step Technique for Low and High Strains and Pressure-Sensing Applications". In: *Small* 11 (2015). DOI: 10.1002/smll.201403532.